

This article is a companion to McKee and Martinson (2020), <https://doi.org/10.1029/2019JC015770>.

**Key Points:**

- On average, half of the intraseasonal velocity variance on the western Antarctic Peninsula shelf can be explained by wind-driven dynamics
- The wind-driven dynamics consist of a wavenumber zero mode and at least two barotropic shelf wave modes
- The large-scale barotropic dynamics lead to upwelling of warm water at a coastal canyon head

**Supporting Information:**

- Supporting Information S1

**Correspondence to:**

D. C. McKee,  
[dcm2xp@virginia.edu](mailto:dcm2xp@virginia.edu)

**Citation:**

McKee, D. C., & Martinson, D. G. (2020). Wind-driven barotropic velocity dynamics on an Antarctic shelf. *Journal of Geophysical Research: Oceans*, 125, e2019JC015771. <https://doi.org/10.1029/2019JC015771>

Received 11 OCT 2019

Accepted 25 FEB 2020

Accepted article online 6 APR 2020

## Wind-Driven Barotropic Velocity Dynamics on an Antarctic Shelf

Darren C. McKee<sup>1,2,3</sup>  and Douglas G. Martinson<sup>1,2</sup> 

<sup>1</sup>Division of Ocean and Climate Physics, Lamont-Doherty Earth Observatory of Columbia University, Palisades, NY, USA, <sup>2</sup>Department of Earth and Environmental Sciences, Columbia University, New York, NY, USA, <sup>3</sup>Now at Department of Environmental Sciences, University of Virginia, Charlottesville, VA, USA

**Abstract** Reanalysis surface stress around the Antarctic continent is used to obtain the cross-shelf sea surface height (SSH) gradient from the shallow water equations in the long-wave limit, and the result is compared to the observed barotropic current sampled by current meters on the western Antarctic Peninsula shelf. Similar to the dynamics of SSH, intraseasonal velocity fluctuations (periods 3–100 days) largely consist of a circumpolar-coherent wavenumber zero mode and of barotropic shelf waves; however, an important distinction from previous studies is the importance of second mode barotropic shelf waves in the velocity signal. Fluctuations with period 40–60 days are particularly energetic. This is partly due to strong fluctuations in the wavenumber zero mode at this period, as previously demonstrated in Drake Passage transport, but also due to excitement of the second mode barotropic shelf wave. After diagnosing the wind-driven dynamics, some of their implications for shelf-slope exchange are discussed. Firstly, it is shown that wintertime upwelling of warm water at a coastal canyon head is associated with a coastal SSH drop. Secondly, it is argued that the waves' subtle baroclinicity over the steep continental slope modifies isopycnal depth and affects shelf access to warm water.

**Plain Language Summary** An existing set of theoretical equations forced by winds along the Antarctic coastline is used to calculate the depth-averaged current on the western Antarctic Peninsula shelf, and the result is compared to that measured by current meters. It is found that current variability on time scales longer than a few days but shorter than a season can be explained by the component of the winds that is uniform around the Antarctic continent summed with current variability generated by the winds over and east of the peninsula. Current variations with periods 40–60 days are particularly energetic and are driven by the component of the winds that is uniform around the continent in addition to winds in the southeastern Pacific sector. The large-scale, wind-driven fluctuations lead to upwelling of warm, deep water at the head of a coastal canyon.

### 1. Introduction

Mid-depth and bottom waters on the western Antarctic Peninsula (WAP) shelf are warming (Martinson et al., 2008; Schmidtko et al., 2014), and marine-terminating glaciers in contact with warm subpycnocline waters are retreating (Cook et al., 2016). These results may be due to a change in the boundary condition at the shelf break (e.g., warmer and/or shoaled subpycnocline waters), an increased transport of mass across the continental slope, or a combination of the two. The magnitude and direction of the long-shore current are important in driving exchange across the continental slope since stronger eastward flows lead to increased flow-topography interaction with bathymetric irregularities (Dinniman & Klinck, 2004; St-Laurent et al., 2013; McKee & Martinson, 2020) and to the development of arrested bottom Ekman layers (Spence et al., 2017; Wåhlin et al., 2012). Each of these processes is asymmetric (different response for eastward versus westward flow) and potentially nonlinear, suggesting the need to understand variance in the long-shore flow in addition to the mean.

There is a gap in our understanding of the dynamics of shelf currents around the Antarctic margins at intra-seasonal time scales (hereafter periods 3–100 days). At time scales of less than one to a few days, several studies point to the importance of near-resonant, short coastal trapped waves (CTW) that may be forced by short-duration wind events (Wåhlin et al., 2016), dense water overflows (Jensen et al., 2013), or tides (Middleton et al., 1987). Kelvin waves also influence sea surface height (SSH) at high frequency (Kusahara & Ohshima, 2014) and are simulated to rapidly transmit remotely generated SSH perturbations

in numerical models (Spence et al., 2017; Webb et al., 2019). However, on longer time scales, while robust statistical links between the long-shore wind stress and long-shore currents have been established in regional numerical models (Dinniman et al., 2011, 2012; Thoma et al., 2008) and observations (e.g., Assmann et al., 2013; Wählin et al., 2013; McKee & Martinson, 2020), there is not yet an agreed-upon dynamical framework to quantitatively explain current fluctuations.

McKee and Martinson (2020) demonstrated the existence of a large-scale (hundreds of kilometers), spatially coherent circulation pattern on the WAP shelf that is associated with an increase in the long-shore flow speed, is strongly barotropic, and is well correlated to the long-shore wind stress. Their findings motivate us to consider that fluctuations in the long-shore flow around Antarctica are driven by low-wavenumber fluctuations in the coastal SSH. The dynamics of low-frequency, low-wavenumber SSH variations around Antarctica are now relatively well understood. Kushahara and Ohshima (2009) used a barotropic model and tide gauge data to show that sea level fluctuations at periods longer than about 10 days are dominated by a circumpolar-coherent wavenumber zero ( $k = 0$ ) response whereas fluctuations at periods of 15, 7.5, and 5 days are dominated by barotropic shelf waves (BSW) that resonate with westward propagating atmospheric variability. However, it is not known to what extent these fluctuations translate into long-shore velocity fluctuations. Bottom pressure in Drake Passage correlates with coastal SSH variability on intraseasonal time scales at short time lag (Hughes et al., 2003), but the open-ocean dynamics of the ACC associated with the wavenumber zero variability (Hughes et al., 1999; Weijer & Gille, 2005) are not necessarily of primary importance along the shelf break where other coastal-trapped phenomena may be relevant.

In this study, we test the hypothesis that long-shore velocity fluctuations along the Antarctic shelf are in geostrophic balance with a wavenumber zero SSH variation and the sum of multiple BSW modes by making use of an array of moored current meters deployed on the WAP continental shelf as part of the Palmer Long Term Ecological Research project (Pal LTER). After presenting the theoretical background, data sources, and methodology (sections 2–4, respectively) we diagnose the regional bathymetry and wave modal properties (section 5.1). We then seek the signature of wavenumber zero variability through empirical orthogonal function (EOF) analysis of the current meter time series and subsurface pressure time series from around the continent (section 5.2). Having shown that the unstratified, nondispersive long-wave limit of BSW is a good approximation for the more general CTW on intraseasonal time scales, we utilize a representative bathymetric profile and reanalysis surface stress to predict time series of long-shore current at the mooring sites using the analytical framework of Gill & Schumann (1974, hereafter GS74), explaining on average about half of the variance (section 5.3). These predictions reveal a previously unreported importance of the second mode BSW and the importance of a 40- to 60-day period in the total velocity variance. In addition to explaining these findings (sections 6.1 and 6.2), we discuss some of their implications for shelf-slope exchange (sections 6.3 and 6.4) before concluding (section 7).

## 2. Theory

### 2.1. Wavenumber Zero Variability

The circumpolar waveguide of the Antarctic coast and a nearly annular atmospheric forcing allow for wavenumber zero variability in coastal SSH. Studies of tide gauges around the continent demonstrate a coherent response at periods longer than 10 days (Aoki, 2002; Hughes et al., 2003; Kushahara & Ohshima, 2009; Matthews & Meredith, 2004), which is shown to correlate significantly to barotropic ACC transport in Southern Drake Passage (Hughes et al., 2003; Matthews & Meredith, 2004) and to indices of the Southern Annular Mode (SAM; Aoki, 2002; Hughes et al., 2003), but more precisely to winds below the latitudes of Drake Passage and close to the Antarctic continent (Hughes et al., 1999; Kushahara & Ohshima, 2009). The wavenumber zero SSH response is a free mode (or a “nearly free mode”; Hughes et al., 1999) that can be excited by winds at any frequency, and the negligible time lag between forcing and ocean response suggests it is strongly damped (Weijer & Gille, 2005). Altimetry data suggest that wavenumber zero winds cause a quasi-instantaneous, Ekman-induced exchange of mass across the continental slope (the free mode) as well as a delayed exchange of mass between the subtropics and the southern ocean; however, only the former projects significantly onto the surface geostrophic flow (Naveira Garabato et al., 2019).

Kushahara and Ohshima (2009) considered the inviscid, nondivergent shallow water equations in a re-entrant channel (long-shore in the  $x$  direction) in order to model wavenumber zero variability.

Uniform variability requires terms with  $\partial/\partial x$  go to zero and requires the offshore mass flux be constant in the long-shore dimension. Further, the boundary condition at the coast requires no mass flux there. These requirements reduce the set of shallow water equations to

$$\left(\frac{\partial}{\partial t} + r_t\right) \frac{d\eta}{dy} = -\frac{f}{g\rho_0 H} \tau^x, \quad (1)$$

which when subject to sinusoidal forcing  $\tau^x = \tau_0(\omega)\sin(\omega t + \theta)$  has solution

$$\eta(y, t) = \eta(L, t) + \frac{f\tau_0}{g\rho_0 \sqrt{r_t^2 + \omega^2}} \int_L^y \frac{1}{LH} \cos(\omega t + \theta + \text{atan}(r_t/\omega)) dy. \quad (2)$$

Given a representative cross-slope bathymetry profile  $H(y)$  and a choice of damping parameter  $r_t$ , this equation can be used to predict the SSH response (and associated geostrophic current) to wavenumber zero wind stress.

## 2.2. BSW in the Long-Wave Limit

The long-shore current on continental shelves is often correlated to the long-shore wind stress (Gill, 1982), and BSW are the natural response to wind forcing in an unstratified ocean: As the wind induces an Ekman transport across the sloping shelf, the associated vorticity anomaly causes the disturbance to propagate with the coast to its left in the southern hemisphere. Observations and theoretical arguments suggest that the shelf wave response consists of a highly rotary, resonant short-wave response to impulsive wind events, and a long-wave response to lower frequency wind stress with small phase lag (Gordon & Huthnance, 1987). We employ the model of GS74, who considered low-frequency ( $\omega \ll f$ ), long-wave ( $L_{\text{shelf}}k \ll 1$ ), wind-driven SSH variability on the continental shelf. Their model considers the shallow water equations forced by the long-shore ( $x$ ) wind stress (without cross-shore variation) in the long-wave limit and assumes a continental slope that varies only in the cross-shore ( $y$ ) dimension.

Assuming nondivergence, we construct a streamfunction  $[Hu, Hv] = [-\partial/\partial y, +\partial/\partial x]\psi$ , which reduces the shallow water equations to the forced vorticity equation

$$\frac{\partial^2}{\partial y \partial t} \left( \frac{1}{H} \frac{\partial \psi}{\partial y} \right) - \frac{f}{H^2} \frac{dH}{dy} \frac{\partial \psi}{\partial x} = \frac{1}{H^2} \frac{dH}{dy} \frac{\tau^x}{\rho_0}. \quad (3)$$

After separating variables, the streamfunction can be expressed as the sum of free wave modes

$$\psi(x, y, t) = \sum_n \varphi_n(x, t) F_n(y), \quad (4)$$

which are obtained from the eigenvalue problem

$$\frac{d}{dy} \left( \frac{1}{H} \frac{dF}{dy} \right) + \frac{1}{cH^2} \frac{dH}{dy} F = 0, \quad (5)$$

whose eigenvalues are one over the phase speed  $c_n$  and whose eigenvectors  $F_n(y)$  define the wave structures, subject to the boundary conditions  $F(0) = 0$  (no normal flow at the coast) and  $dF(L)/dy = 0$  (no long-shore flow at the oceanic edge). The wave structures and phase speeds are easily obtained numerically given a bathymetry profile  $H(y)$  and are used to compute the wind coupling coefficients,

$$b_n = \int_0^L \frac{1}{H^2} \frac{dH}{dy} F_n(y) dy. \quad (6)$$

The wave amplitudes are determined from the spectrum of forced wave equations,

$$\frac{1}{c_n} \frac{\partial \varphi_n}{\partial t} + \frac{\partial \varphi_n}{\partial x} + \underbrace{r_n \varphi_n}_{\text{damping}} = - \frac{b_n}{f \rho_0} \tau^x(x, t) \quad (7)$$

to which we have added a linear damping term, following GS74. The solution at location  $x = 0$  and time  $t$  is

$$\varphi_n(0, t) = - \frac{b_n}{f \rho_0} \int_{x_{\text{inf}}}^0 \exp(-r_n x') \tau^x \left( x', t + \frac{x'}{c_n} \right) dx', \quad (8)$$

where integration is carried out along a characteristic, in the direction of wave propagation, to the observation site  $x' = 0$  from some point  $x_{\text{inf}}$  where wave amplitude is negligible.

In summary, given a bathymetry profile and surface stress data, one can use equation 5 to derive the wave properties, equation 8 to compute the wave amplitudes, and equation 4 to construct the dimensional streamfunction. From the definition of the streamfunction, we can back out the dimensional barotropic current and, assuming geostrophic balance, compute the SSH anomaly. On many shelves, sufficient signal can be explained with only the first mode (Brink, 1982a; Gordon & Huthnance, 1987; Rivas, 2017; Schulz et al., 2012), although, for reasons discussed later, we consider up to three modes.

The more general CTW are dispersive, are influenced by stratification, and can be modeled with the Boussinesq, hydrostatic equations of motion (e.g., Brink, 2006). Qualitatively, they are hybrids of internal Kelvin waves and BSW and become increasingly bottom trapped as stratification increases (it can be shown that BSW are CTW in the limit of vanishing stratification; Huthnance, 1978). For the Antarctic environment where stratification is weak and for the spectral region we are interested in, the added complexities of a stratified, dispersive model are not necessary. We calculate the CTW modes only to test the aptness of the BSW model.

### 3. Data

#### 3.1. Mooring Data

Predicted velocity signals are compared to hourly moored current meter records collected on the WAP shelf by the Pal LTER program (Martinson, 2020). These are the same data used by McKee and Martinson (2020), and we process them in the same way. Because the moorings are deployed and recovered on annual January cruises, all predictions and comparisons with data are conducted for one “mooring-year,” which is approximately 350 days long. Most deployments contain two or more current meters in the vertical (nominally one each above and below the permanent pycnocline), and for each mooring, all data are reduced to a single measure of “long-shore current,” which is the depth average of the long-shore components. We focus on sites 300.100 and 200.140 (Figure 1b) as they demonstrate strong long-shore variance and have good coverage in the vertical (six current meters at 200.140 in 2013, three current meters at 300.100 in 2012, and two in 2010, 2011, and 2014).

A thermistor mooring at Palmer Station E (Pal E) deployed in mooring-year 2014 is used to assess implications of the barotropic variance for coastal upwelling at a submarine canyon head (Martinson, 2020). The mooring had seven thermistors that nominally spanned 34–146 dbar in the water column, each of which were subsampled once per hour and used to construct 1-dbar temperature profiles at each time step by interpolation with a piecewise cubic Hermite interpolating polynomial. Two of the records (nominally at 85 and 146 dbar) have periodic gaps of about 4.8 days due to EEPROM failures, but these do not affect the quality of the interpolant nor our interpretation of the data.

#### 3.2. Reanalysis and Climatology Data

We use surface stress and surface pressure from the ECMWF ERA-Interim reanalysis (European Centre for Medium-range Weather Forecast, 2011). The former is used to force our predictions, and the latter is used to correct tide gauge records for the inverse barometer effect. Both are reported on a  $0.75^\circ$  grid at a temporal interval of 12 hr. While the surface pressure is a true reanalysis variable, the surface stress is technically a forecast variable, representing the downward turbulent stress at the surface accumulated over a 12-hr forecast. As such, we divide the surface stress by the time step and assign each value a new time stamp corresponding to the middle of the forecast window.

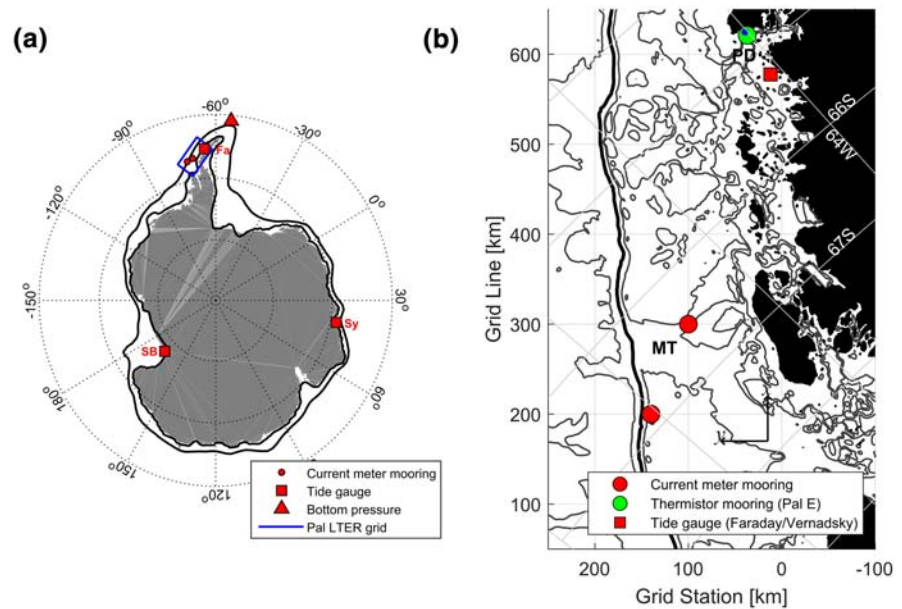


**Figure 1.** Overview of the physical setting. (a) Map of the Antarctic continent defined by the 0 m isobath in ETOPO5 (gray shading) along with the Continental Shelf Break and Coast Contours (black lines; see section 3.4). Lines of latitude are indicated every 10°. The two current meter moorings (red circles), the single Drake Passage South bottom pressure sensor (red triangle), and the three tide gauges (red squares; Fa = Faraday/Vernadsky, Sy = Syowa, SB = Scott Base) are indicated. The Pal LTER sampling grid is enclosed by a blue rectangle. (b) Inset showing the Pal LTER grid. Locations are generally referred to with the LTER coordinate system and are given as GGG.SSS where GGG is the grid line and SSS the grid station (each in kilometers). Locations of Marguerite Trough (MT), Palmer Deep (PD), and Palmer Station (blue dot near the thermistor mooring) are indicated.

Statistically analyzed, climatological ocean data from the World Ocean Atlas 2018 (Locarnini et al., 2018; Zweng et al., 2018) are used to construct a circumpolar, coastal stratification profile for use when calculating CTW modal structures. We use the annual climatology product that objectively analyzes all decades on a 0.25° grid.

### 3.3. Subsurface Pressure Measurements

We acquire tide gauge data from Faraday (now Vernadsky), Syowa, and Scott Base (Figure 1a) from the University of Hawaii Sea Level Center (Caldwell et al., 2015). These are Research Quality records distributed on an hourly time step. Short-period (semidiurnal and diurnal) tides identified with a signal-to-noise ratio (SNR) greater than 1 are removed via harmonic analysis (Pawlowicz et al., 2002). To correct for the inverse barometer effect, the reanalysis surface pressure data are spatially interpolated onto the tide gauge site (with a bicubic spline) at each reanalysis time step and then interpolated in time (with a linear interpolant) onto the hourly tide gauge grid. Then, the interpolated surface pressure data are multiplied by the factor (1 cm sea level)/(1 mbar atmospheric pressure) and combined with the tide gauge signal. Because long-period tides (fortnightly and longer) have low amplitude compared to weather-band variability, we enhance SNR by examining the multiyear, inverse barometer-corrected records, which reduce noise by distributing nontidal variance among more Fourier harmonics. We find Ssa, Mm, and Mf to exhibit SNR greater than 1, and they are removed by harmonic analysis (Pawlowicz et al., 2002). Finally, small gaps are filled by linear interpolation, and a low-pass filter with cutoff period of 2 days is applied.

Tide gauge data are complemented by bottom pressure data from southern Drake Passage (Drake Passage South Deep, hereafter DPS; 1,980 m depth in 2009–11, 1,920 m in 2011–13; Figure 1a) acquired from the Permanent Service for Mean Sea Level (National Oceanography Centre, 2015). These data are already detided for short-period tides so we remove only Ssa, Mm, and Mf via harmonic analysis as described above. They are interpolated where appropriate and low-pass filtered as above.

### 3.4. Bathymetry

Bathymetry is derived from the ETOPO5 product (National Geophysical Data Center, 1988), which reports surface elevation values on a 5-min grid. We use ETOPO5 in place of the newer ETOPO1 since we need a smoothed representation of the coastal profile, and details of small-scale bathymetric features are not important for large-scale ocean variability (see Section S1 in the supporting information). To locate the continental shelf break, the 5-min data are bin-averaged into ( $2^\circ$  longitude,  $1^\circ$  latitude) bins and then smoothed again by averaging each cell with its neighboring 8 cells. On the resulting grid, cells with bottom depth shallower than 100 m are set to 0 m and treated as land. From this smoothed database, we extract the location of the 1,500 m isobath to define the Continental Shelf Break Contour. To locate the coast, the smoothing procedure is repeated as above except the values are gridded onto ( $1^\circ$  longitude,  $0.5^\circ$  latitude) bins before averaging with their neighboring values, and this finer database is used to extract the location of the 100 m isobath, which defines the Coast Contour. Both contours are shown in Figure 1a.

## 4. Methods

### 4.1. Characterizing the Physical Environment

The physical environment defines the waves' modal properties and, along with the wind stress, their amplitude. It includes a representative bathymetry profile  $H(y)$ , a coastal pathway with long-shore wind stress defined at each location  $x$  around the continent, and a stratification profile. The Continental Shelf Break Contour is discretized into 100 evenly spaced segments and is used to define a bathymetry profile  $H_i(y)$  and a long-shore wind stress value  $\tau^x(x_i, t)$  at each location  $x_i$  around the continent (approx. 167 km apart) as described in Section S1 and Figure S1. We define our Circumpolar bathymetry profile as the average of all  $H_i(y)$  in  $0\text{--}150^\circ\text{E}$  or  $200\text{--}300^\circ\text{E}$  where we have excluded the Weddell and Ross Seas. We also construct a local WAP profile by averaging the profiles for segments in  $280\text{--}300^\circ\text{E}$ . Each  $H(y)$  is defined out to  $y = 800$  km ( $y = 0$  is the coast).

Stratification associated with the Circumpolar bathymetry profile is computed from the World Ocean Atlas 2018 by isolating all temperature and salinity profiles in the same longitudinal domain used to define the averaged bathymetry profile (with bottom depth shallower than 3,000 m), computing potential density on those profiles, averaging them on their native depth levels, and finite differencing the composite profile to compute buoyancy frequency  $N(z)$ . For the WAP profile, we use the shelf-averaged  $N^2$  profile from McKee et al. (2019), but to avoid overturns  $N(z)$  at all depths shallower than 24 m is set to the value at 24 m.

### 4.2. Wave Modal Analyses

All modal analyses evaluate  $f$  at  $67^\circ\text{S}$  and consider four bathymetric profiles: (1) Circumpolar profile, (2) Circumpolar profile with bottom depth capped at 4,000 m, (3) WAP profile, and (4) WAP profile with bottom depth capped at 4,000 m. The BSW modal properties are obtained numerically from equation 5 and assume a uniform density  $\rho_0 = 1,027$  kg m $^{-3}$ . The CTW modal properties are obtained numerically with the inviscid `bigr*.m` software (Brink, 2006). The model grid is discretized into 80 cross-shore and between 40 and 44 vertical points (depending on maximum bottom depth), which ensures accurate representation of the cross-slope bathymetry and of the major features of the stratification, respectively. The model is run with a rigid lid, a closed boundary at the coast, and an open boundary at the seaward edge.

### 4.3. Detection and Prediction of Wavenumber Zero Variability

#### 4.3.1. Detection

Circumpolar-coherent, wavenumber zero variability is identified via EOF decomposition of the lag-zero covariance within the array of circumpolar tide gauge series in years 2011 and 2012, which afford the greatest coverage around the continent (Table 1). The time series at each site are reconstructed using EOF1 alone and then averaged to obtain a single index of dimensional, coastal wavenumber zero variability.

#### 4.3.2. Prediction

The wavenumber zero amplitude and phase of the long-shore stress at each frequency are extracted via a 2D Fourier Transform. A time series of wavenumber zero variability is calculated from equation 2. In the integral, we assume  $L = 450$  km as this is where the bathymetry becomes substantially flatter. This parameter affects only the amplitude of the prediction and not its phasing. For the damping parameter, we set  $r_t^{-1}$

**Table 1**  
Data Coverage for Each Mooring-Year

	300.100	200.140	Faraday/ Vernadsky	Syowa	Scott Base	DPS
2008	x		x	x		
2010	x		x			x
2011	x		x	x	x	x
2012	x		x	x	x	x
2013		x	x	x		x
2014	x			x		
2017	x					

Note. Only years with current meter data at one of 300.100 or 200.140 are considered. Tide gauge series with gaps larger than 11.5 days are not used. With this threshold, Faraday/Vernadsky has one gap of 1.4 days while Scott Base is most affected with 12 gaps (largest 11.5 days).

= 5 days because this value yields both good phase agreement with the observations and good results for the prediction of the BSW (see below).

#### 4.4. Prediction of BSW

To compute BSW amplitude at  $x_0$  with equation 8, the long-shore stress at  $x_i$  is lagged by the mode-dependent time lag  $T_n(x_i) = (x_i - x_0)/c_n$ . Stress at the appropriate lag is calculated from the gridded data by interpolation in time with a cubic Hermite interpolating polynomial. To acknowledge the periodic domain, the wind-wave pathway is unwrapped and duplicated twice around the continent. A 2D ideal filter is used to remove wavenumber zero variability from the wind stress space-time series, to impose a high-frequency cutoff  $(3 \text{ day})^{-1}$  so that the first mode BSW is approximately nondispersive, and to impose a low-frequency cutoff  $(100 \text{ day})^{-1}$  to retain the full spectrum of intraseasonal variability. To compare the data to the predictions, they are linearly interpolated (effectively sub-

sampled) onto the 12-hr reanalysis grid. Predictions are made at 300.100, 200.140, and at Faraday/Vernadsky tide gauge, where we have data with which to evaluate them. Predictions of velocity are evaluated at the location of the 450 m isobath (which represents a typical mooring depth), and predictions of SSH are evaluated at the coast ( $y = 0$ ).

In equation 8, the damping coefficient  $r_n = r_i c_n^{-1}$  varies for each mode: Higher (slower) modes are damped more than lower (faster) modes. As this parameter serves as the  $e$ -folding length for the lagged wind stress, it indicates that higher modes are increasingly dependent on local wind stress. We find  $r_i^{-1} = 5$  days yields good results for BSW amplitude and phase and use that value throughout. Importantly, we have followed GS74 by simply adding a linear damping term to the wave equations as opposed to formally including attenuation in the original model. More sophisticated treatments model damping with a bottom Ekman layer friction (Brink, 1982b; Brink & Allen, 1978). In such cases, because the bottom stress depends on the variable bottom depth, friction causes energy to be scattered among modes, coupling them together in a manner that is not considered here (nor by GS74). Treatment of damping by GS74 is empirical and represents attenuation by any process related to dissipation, scattering, or morphological changes in the continental slope. Waves may be scattered, for example, by rapidly turning coastlines or other topographical irregularities (Griffin & Middleton, 1986). The sharply turning coastline at Drake Passage and obstruction by the South Shetland Islands may impact propagation in ways comparable to the effects of friction leading us to choose the more general approach of GS74.

## 5. Results

### 5.1. Modal Structures and Validity of the Barotropic and Long-Wave Assumptions

The BSW and CTW dispersion relations are shown in Figure 2, and the bathymetry profiles and the modal structures are shown in Figures 3 and 4. The circumpolar profile (Figure 3) does not exhibit a very prominent continental shelf. The major continental slope is within about 450 km from the coast. The dispersion relation suggests that BSW and CTW properties agree well in the long-wave limit, certainly for wavenumbers  $k \leq 3$  (Figure 2a). While there is not a clear shelf break for this profile, the first mode ( $n = 1$ ) BSW structure for SSH is largest near the coast (Figure 3a), and the corresponding velocity structure is of uniform sign (Figure 3b). The second mode ( $n = 2$ ) SSH has a maximum over the steepest part of the continental slope (Figure 3a), and thus the velocity structure changes sign there (Figure 3b). The CTW modal structures are essentially unstratified over the entire domain and have the same inflection points as the BSW modes (Figures 3c–3f). Note that unlike the CTW, the BSW structures go to zero at the seaward boundary because integration of the geostrophic balance actually gives the SSH anomaly relative to that at the seaward boundary, which we have assumed is zero.

The WAP profile (Figure 4) has a well-defined continental shelf of ~150 km width adjacent to a steep continental slope, followed by a more gradual roll-off. The profile reaches 4,000 m depth at about 500 km from the coast and continues falling to ~4,400 m at 800 km from the coast. The phase speeds for the WAP bathymetry are faster (Figure 2c). This is consistent with the continental shelf being more pronounced, with a

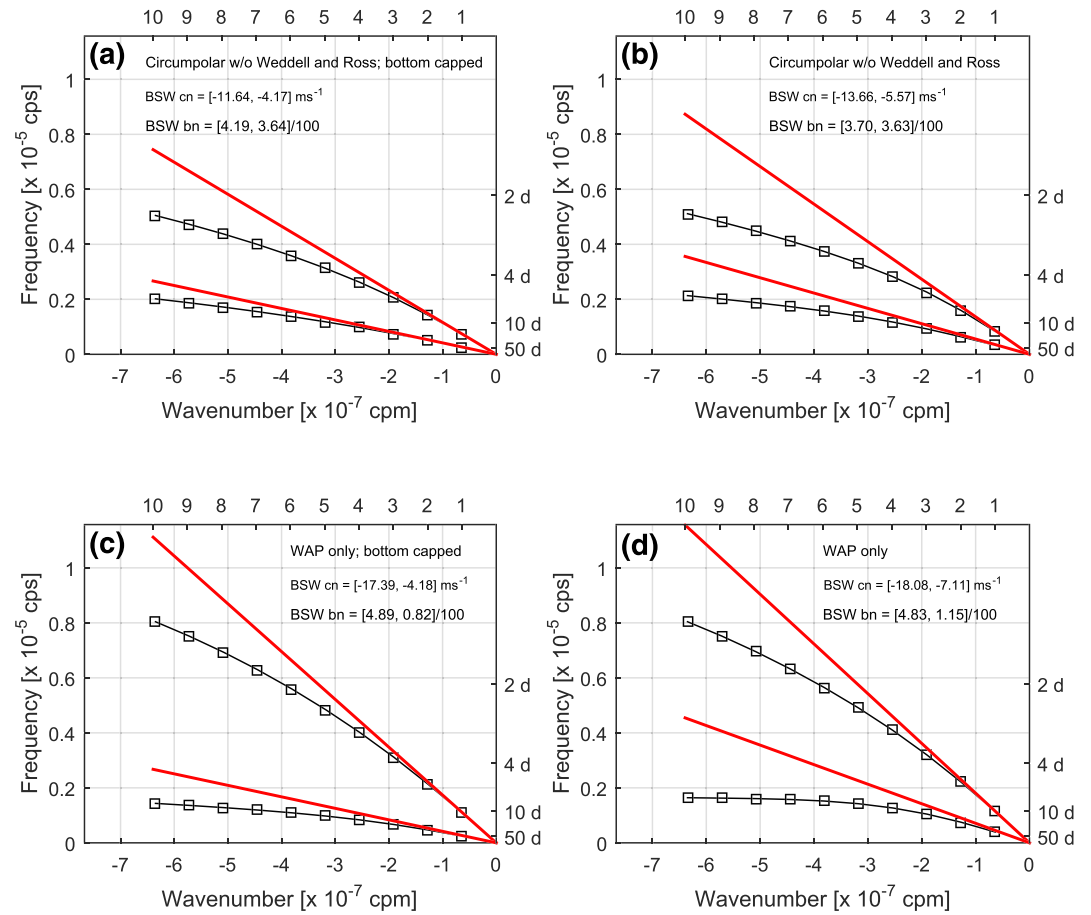


**Figure 2.** Dispersion relations for BSW (red lines) and CTW (black squares) for the first two wave modes for a variety of shelf profiles. The additional horizontal axis (above) indicates wavenumber as a fraction of the circumpolar distance, and the additional vertical axis (right) indicates period in days. See section 2.2 for definitions of  $c_n$  and  $b_n$ . (a) Circumpolar profile with bottom depth capped at 4,000 m; (b) Circumpolar profile; (c) WAP profile with bottom depth capped at 4,000 m; (d) WAP profile.

wider shelf and steeper slope (Huthnance, 1978). Again, the BSW and CTW agree well in the long-wave limit, at least for wavenumbers  $k \leq 3$ . The first mode BSW structure for SSH has amplitude confined to the continental shelf (Figure 4a) and, consequently, the first mode velocity structure has approximately uniform amplitude over the shelf (Figure 4b). The second mode SSH structure has largest amplitude over the steepest part of the slope (Figure 4a) meaning that the second mode velocity changes sign there (Figure 4b). Much like the case of the circumpolar profile, the CTW modes are essentially unstratified, and their inflection points mirror those of the BSW, with the exception that baroclinicity over the continental slope is more pronounced than it is for the Circumpolar profile, leading to weak bottom trapping there (Figure 4e). For the WAP, stratification in and above the permanent pycnocline and maximum bottom slope  $\alpha$  are larger than the Circumpolar average. Baroclinicity of CTW depends on their combined influence through the Burger number (Huthnance, 1978, 1981)

$$\text{Bu} = \left(\frac{NH}{fL}\right)^2 = \left(\frac{N\alpha}{f}\right)^2. \quad (9)$$

For both bathymetry profiles, modal properties vary slightly when allowing the bathymetry to fall to its natural bottom depth at the domain edge (800 km) versus when capping it at 4,000 m. In general, not capping the bottom depth has the effect of increasing the phase speeds (compare Figures 2a and 2c to Figures 2b and 2d) and “dragging” the modal structures seaward (not shown). These effects are more pronounced for higher mode waves ( $n > 1$ ) and for the Circumpolar profile, likely because that profile does not have a well-defined

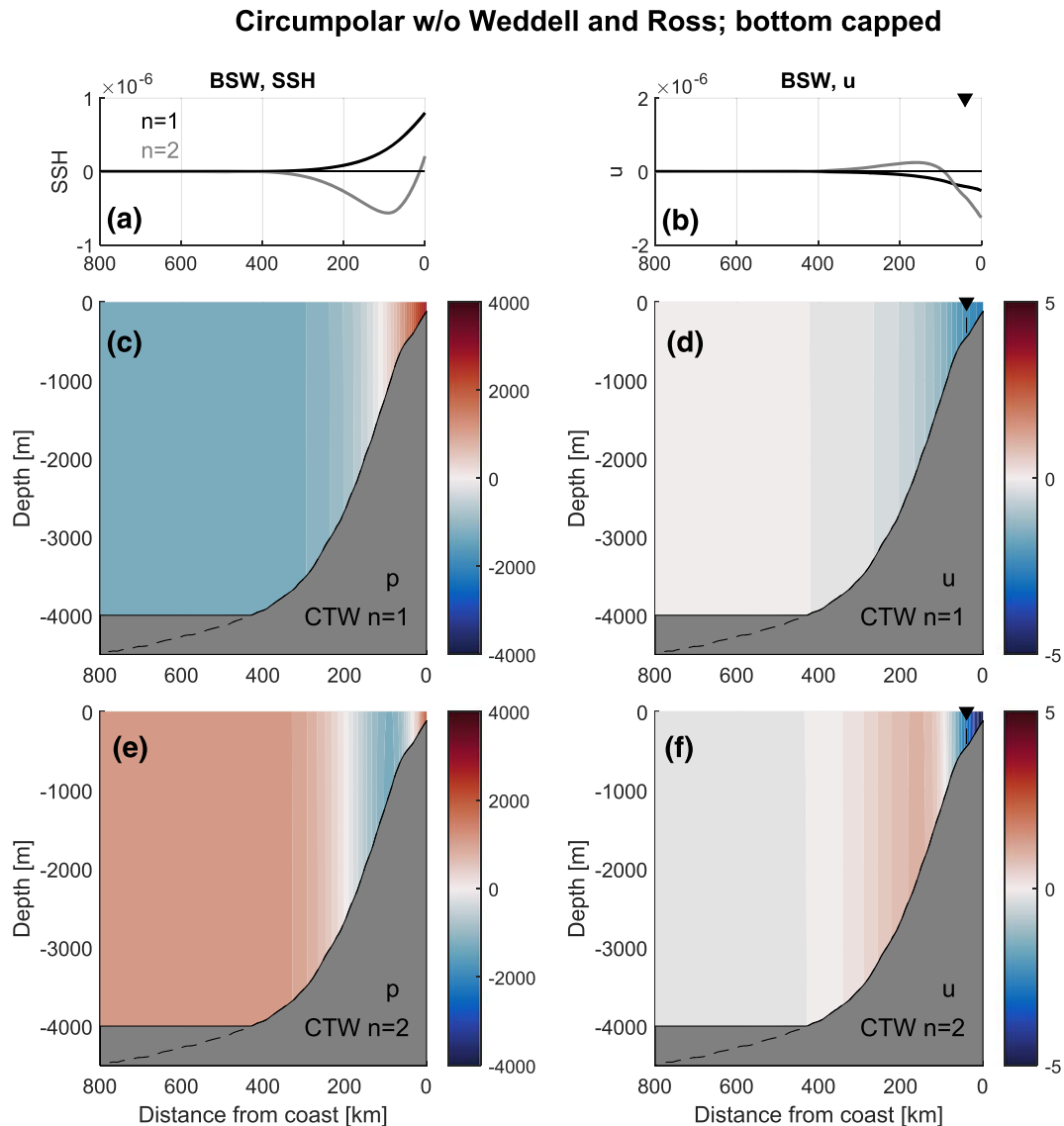


**Figure 3.** BSW and CTW modal structures for the circumpolar, bottom-capped profile. All amplitudes are arbitrary until scaled by appropriate coupling coefficients and surface stress. The black wedge indicates a typical mooring location. (a) Modal SSH for the first two BSW. (b) Modal long-shore current for the first two BSW. (c) Modal pressure for the first CTW. (d) Modal long-shore current for the first CTW. (e) Modal pressure for the second CTW. (f) Modal long-shore current for the second CTW. In panels (c)–(f), the actual bottom depth is shown with a dashed black line.

continental shelf break and associated vorticity gradient to “anchor” the modes. The reason why modal amplitude persists far from the coast is because the seaward boundary condition is for no long-shore flow at the edge of the domain. So as long as there is a bathymetry gradient, however far from the coast, there will be modal amplitude. It is not clear how realistic that behavior is. In any circumstance, a choice must be made when preparing a bathymetry profile. We use the bottom-capped circumpolar profile in all predictions, although we will consider the range of phase speeds (all four profiles) and possible effects of dispersion when analyzing them. Overall, these results indicate that the waves can be treated as BSW on the continental shelf in the low-frequency range of predictive interest.

### 5.2. Detection of Wavenumber Zero Variability

The depth-averaged long-shore current at 300.100 is plotted in Figure 5a along with all subsurface pressure signals. As indicated in Figure 1a, the three tide gauge records provide a reasonably complete spatial coverage around the continent. On intraseasonal time scales, the series are well correlated to the barotropic

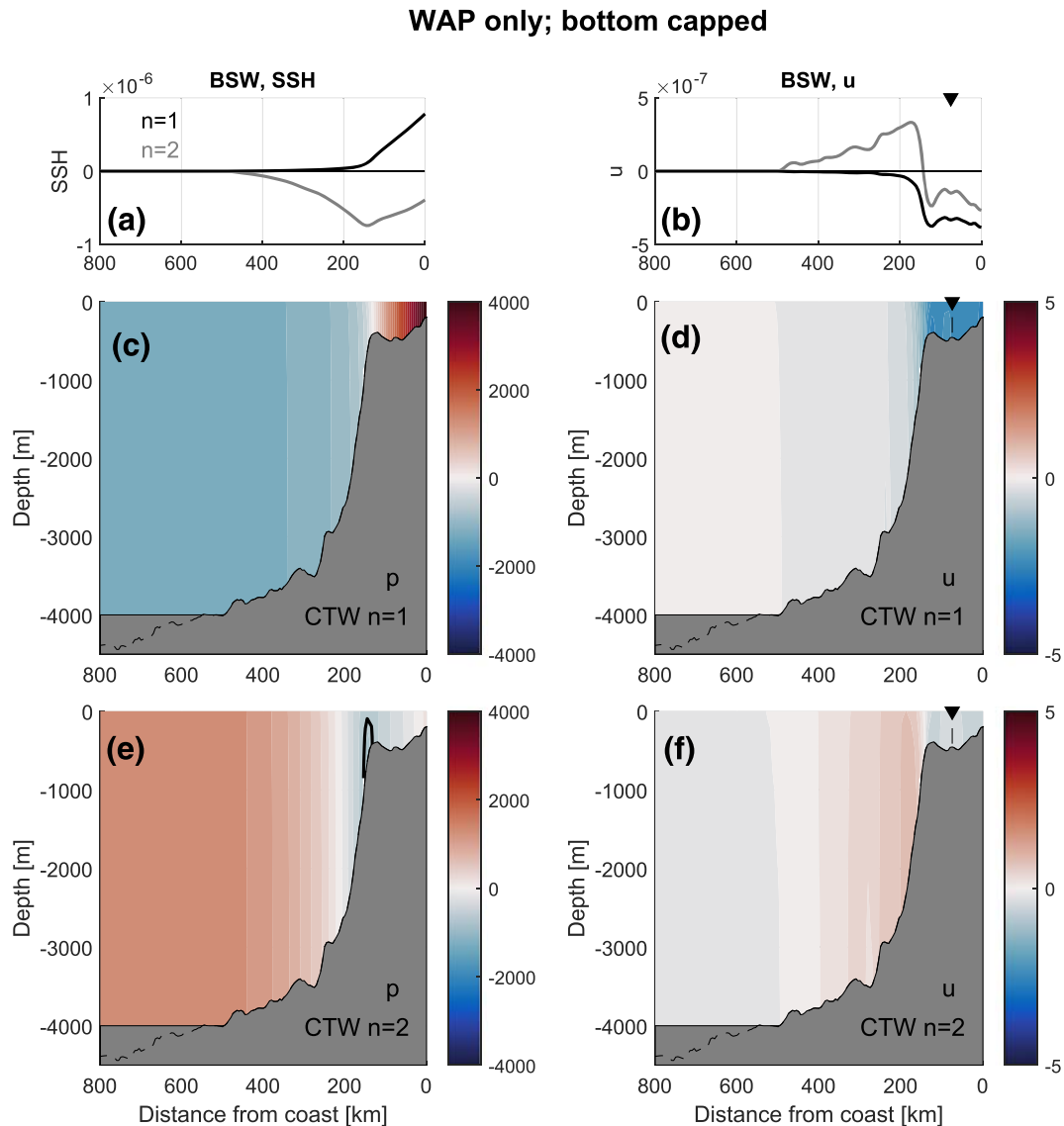


**Figure 4.** As in Figure 3 but for the WAP bottom-capped depth profile. Panel (e) shows an arbitrary black contour to indicate baroclinicity over the slope.

velocity at 300.100 (correlation coefficients indicated in Figure 5a). The correlation is strongest with nearby Faraday/Vernadsky SSH, but the correlations are statistically significant (at the 1% level) with all series. The correlation is clearly dominated by large swings with period 40–60 days, which will be discussed later. At 200.140 (not shown), correlations of long-shore current with available circum-Antarctic subsurface pressure are slightly weaker ( $r$  between 0.18 and 0.54) but still significant, suggesting that wavenumber zero variability may be less important than other processes at the shelf edge.

Significant correlation around the continent (at zero lag) requires that some amount of the velocity variance consists of a wavenumber zero mode, which is identified quantitatively via EOF decomposition of the covariances. We consider a dimensional estimate by decomposing coastal SSH signals only, and we consider a second estimate that takes advantage of all available time series, including the DPS pressure and the current meter series. In each case, the first EOF is of wavenumber zero in the sense that EOF weights are all the same sign. EOF1 explains between 63–67% of the total intraseasonal variance. The two estimates are well correlated to each other ( $r = 0.97$ ) and to 300.100 long-shore current ( $r = 0.71$  and  $0.77$  respectively;  $p \approx 0$ ).

We compare the detected signal to a wind-driven prediction using equation 2. The dimensional estimate is recomputed via EOF analysis using the 2012 tide gauge data band-pass filtered to retain periods of 10–

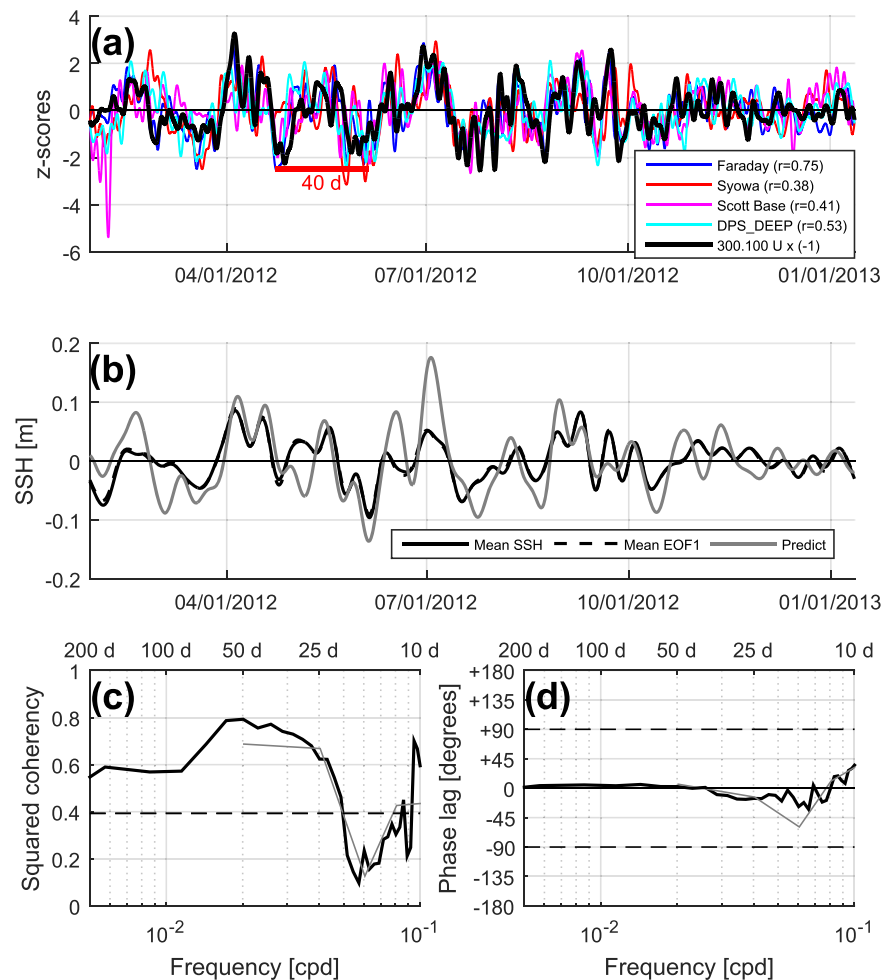


**Figure 5.** Assessment of wavenumber zero variability. (a) Time series of long-shore current at 300.100 year 2012 (times  $-1$ ; bold black) along with the subsurface pressure series (thin colors). All series have been standardized and band-pass filtered to retain periods 3–100 days. Correlation coefficients with long-shore current are indicated in the legend. Dates are given as mm/dd/yyyy. (b) Plot of the prediction against two estimates in the time domain. (c) Squared coherency and (d) cross-phase spectra between the prediction and the first estimate. The bold black spectra utilize multitaper smoothing and the thin gray spectra average nonoverlapping windows, each method yielding 14 effective degrees of freedom (EDOF). The dashed line in (c) is the threshold for significant coherence at a 5% level.

200 days. Then, we reconstruct the SSH at each site from EOF1 only and average all of them, yielding an average amplitude of SSH that is spatially coherent. The detected and predicted series are plotted together in Figure 5b. The two are reasonably well correlated ( $r = 0.69$ ,  $p \approx 0$ ) and their phase lag is negligible where the coherence is significant at the 5% level, suggesting a good choice of damping parameter (Figures 5c and 5d). Analysis of year 2011 (same spatial coverage as 2012) yields similar results ( $r = 0.65$ ,  $p \approx 0$ ).

We have therefore shown that a wavenumber zero mode can be detected from tide gauges only and/or tide gauges along with bottom pressure and current meter series and that the two estimates are similar. The detected wavenumber zero mode explains over 50% of the intraseasonal velocity variance at 300.100 in 2012.

### 5.3. Prediction of Total Signal and Comparison to Data

Predictions include the wavenumber zero mode summed cumulatively with the  $n = 1, 2$ , and 3 BSW and are carried out with the surface stress filtered to retain periods 3–100 days. Correlation coefficients are shown in Table 2, time series of a representative prediction (300.100 year 2012) are shown in Figure 6, and coherency and cross-phase spectra for the same prediction against observations are shown in Figure 7. Overall, the

**Table 2**

Correlation Coefficients for Predictions Against Observations

	$k = 0$ mode	$k = 0 + n = 1$	$k = 0 + n = 1,2$	$k = 0 + n = 1,2,3$
300.100/2008 <sup>b</sup>	0.36	(0.48) 0.59	(0.61) 0.69	(0.63) 0.71
300.100/2010	0.40	(0.37) 0.56	(0.51) 0.66	(0.53) 0.68
300.100/2011 <sup>a</sup>	0.28	(0.34) 0.47	(0.50) 0.60	(0.53) 0.63
300.100/2012	0.65	(0.36) 0.71	(0.55) 0.78	(0.57) 0.79
300.100/2014	0.41	(0.48) 0.63	(0.60) 0.74	(0.61) 0.75
300.100/2017 <sup>b</sup>	0.39	(0.45) 0.57	(0.63) 0.72	(0.65) 0.74
200.140/2013	0.41	(0.30) 0.47	(0.55) 0.66	(0.58) 0.69
Faraday/2008	0.36	(0.24) 0.42	(0.27) 0.43	(0.34) 0.48
Faraday/2010	0.54	(0.26) 0.59	(0.28) 0.60	(0.33) 0.62
Faraday/2011	0.48	(0.26) 0.56	(0.28) 0.57	(0.32) 0.60
Faraday/2012	0.55	(0.31) 0.64	(0.34) 0.65	(0.40) 0.67
Faraday/2013	0.45	(0.36) 0.55	(0.38) 0.57	(0.43) 0.61

Note. Predictions in parentheses involve the wave modes only. All correlations are significant at the 1% level.  
<sup>a</sup>Did not sample below the permanent pycnocline. <sup>b</sup>Derived from only one current meter.

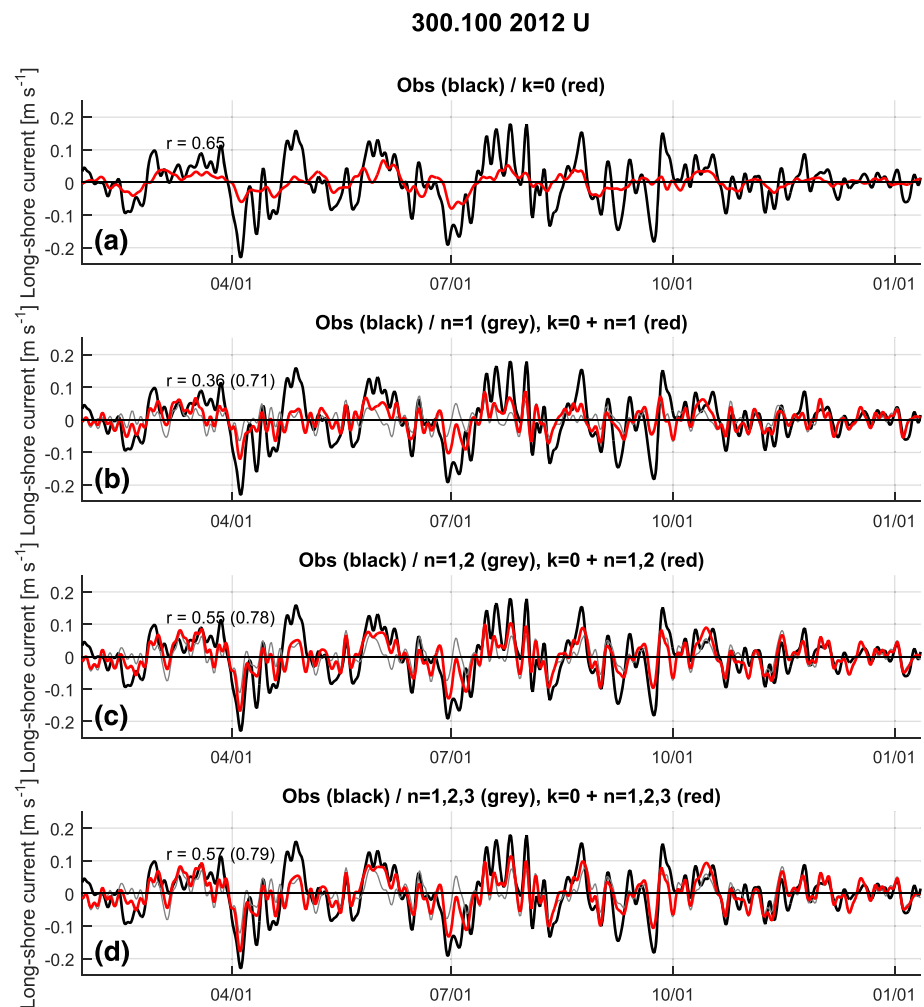


**Figure 6.** Time domain comparison of predicted and measured long-shore current at 300.100 for the year with the best sensor coverage (2012). In each panel, the observations are indicated with a thick black line and the prediction using the wavenumber zero mode plus some number of waves (just the waves) is given as a thick red (thin gray) line. The predictions cumulatively add the (a) wavenumber zero, (b)  $n = 1$ , (c)  $n = 2$ , and (d)  $n = 3$  modes. Dates are given as mm/dd.

300.100 2012 U

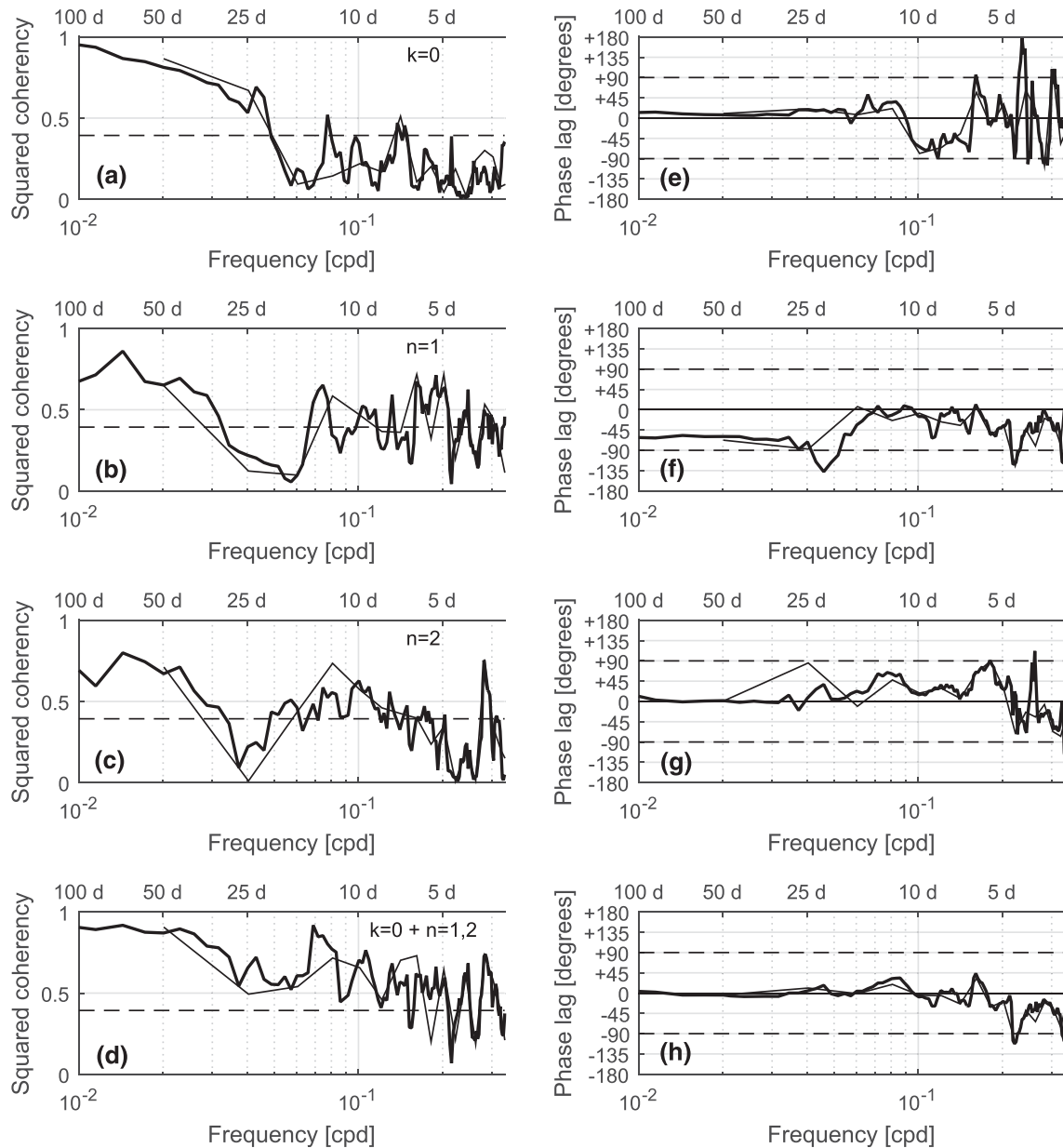


**Figure 7.** Frequency domain comparison of predicted and measured long-shore current at 300.100 for the year with the best sensor coverage (2012). Panels at left (right) show the squared coherency (cross-phase) spectra. The signals retained are labeled in the upper right of the coherency plots. Thick black spectra use the multitaper method and thin spectra average nonoverlapping windows, each with 14 EDOF. The horizontal dashed line indicates coherence significant at a 5% level.

quality of the predictions is good, being able to explain on average about 50% of the velocity variance at 300.100. Inspection of the time series (Figure 6) reveals that, in addition to the phasing between the signals agreeing, thus yielding the positive correlation coefficients, the amplitude of the prediction is remarkably close to the observed. The similarity of the amplitudes lends credence to the physical model representing the appropriate transfer of any covarying wind signal to the ocean. The table and time series reveal that there is generally substantial improvement in the correlation when introducing the second mode BSW, but the third mode BSW contributes little.

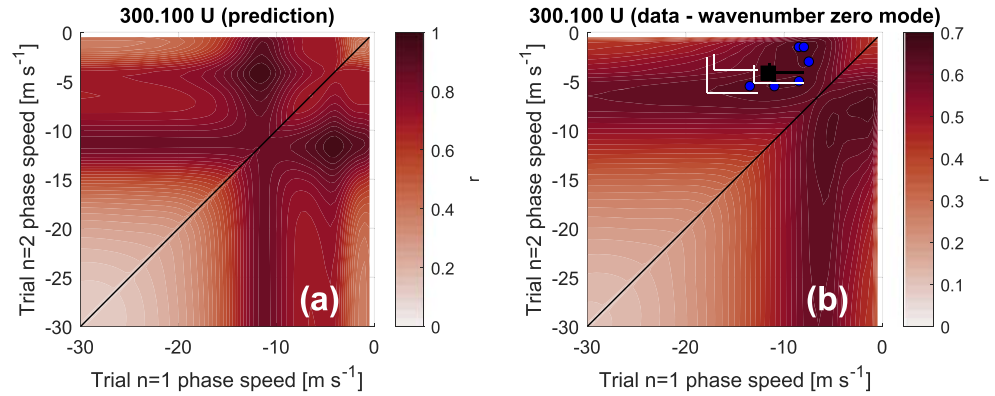


**Figure 8.** Correlation coefficients for the trial predictions (optimal results from equation 10) averaged across all mooring-years at 300.100 (years in Table 1). (a) Correlation coefficients for the optimal fits against the actual wind-driven prediction. (b) Correlation coefficients for the optimal fits against the data minus the predicted wavenumber zero mode. In panel (b), the blue circles indicate the optimal phase speed pairs for each year, the black square indicates the actual BSW phase speed pair for the circumpolar bottom-capped bathymetry, and the L-shaped axes indicate the range of dispersive CTW phase speeds for wavenumbers 1–10 for each bathymetry profile (see Figure 2).

The coherency spectra suggest that the wavenumber zero mode contributes most at periods longer than 20 days (Figure 7a). The first mode BSW is most coherent at periods 5–15 days (Figure 7b) while the second mode is most coherent at periods longer than  $\sim 7$  days (Figure 7c), and the coherency in general seems to increase with decreasing frequency. Phase lags are small where coherency is significant at the 5% level, and by the time the wavenumber zero mode is summed with the first two BSW, coherency is generally significant over the full spectrum (Figure 7d) with small phase lag (Figure 7h), suggesting most of the essential physics have been captured.

The predictions utilize a fixed set of modal structures and phase speeds corresponding to a representative bathymetry profile. To evaluate the quality of the chosen phase speeds, we conduct an iterative procedure that assesses the quality of prediction for arbitrary phase speeds. Specifically, after removing the predicted wavenumber zero mode from the observed time series, we consider pairs of all phase speeds  $-30.0 \text{ m s}^{-1} \leq c_{1,j} < c_{2,j} < 0.0 \text{ m s}^{-1}$  at  $0.5 \text{ m s}^{-1}$  increments and fit the function

$$U_{\text{obs}}(0, t) = \sum_{n=1}^2 \left[ A_{n,j} \int_{x_{\text{inf}}}^0 \exp(-x' r_t / |c_{n,j}|) \tau^x \left( x', t + \frac{x'}{c_{n,j}} \right) dx' \right] + \varepsilon \quad (10)$$

via linear regression, solving for amplitudes  $A_{1,j}$  and  $A_{2,j}$ . For each fit, we compute its correlation coefficient with the observations. The function is also fit at each trial phase speed to our actual wind-driven prediction, and we compute its correlation coefficient as well. The latter evaluates how much spread we should expect to see in the correlation coefficients if the data truly constitute the sum of two BSW. This is done for every mooring-year, and symmetric matrices of correlation coefficient squared as a function of trial phase speeds are computed and averaged together.

Figure 8 shows the averaged correlation coefficients for the trial predictions against the actual prediction (panel a) and the data (panel b). The phase speeds used in the actual prediction (black square) are shown along with the best fit trial phase speeds for each year of data (blue circles). Overall, the plots agree very well. The contours on each plot have the same sense, with two very fast or two very slow waves fitting poorly, for example. The trial fits to data do not separate into two ridges like the trial fits to the actual prediction do. There is some evidence that the phase speeds corresponding to WAP bathymetry (left-most two gray axes) fall on the ridge of high correlation coefficient, but they are not as close to the optimal pairs of trial phase speeds as are the circum-Antarctic phase speeds (right-most gray axes and black square and axes).

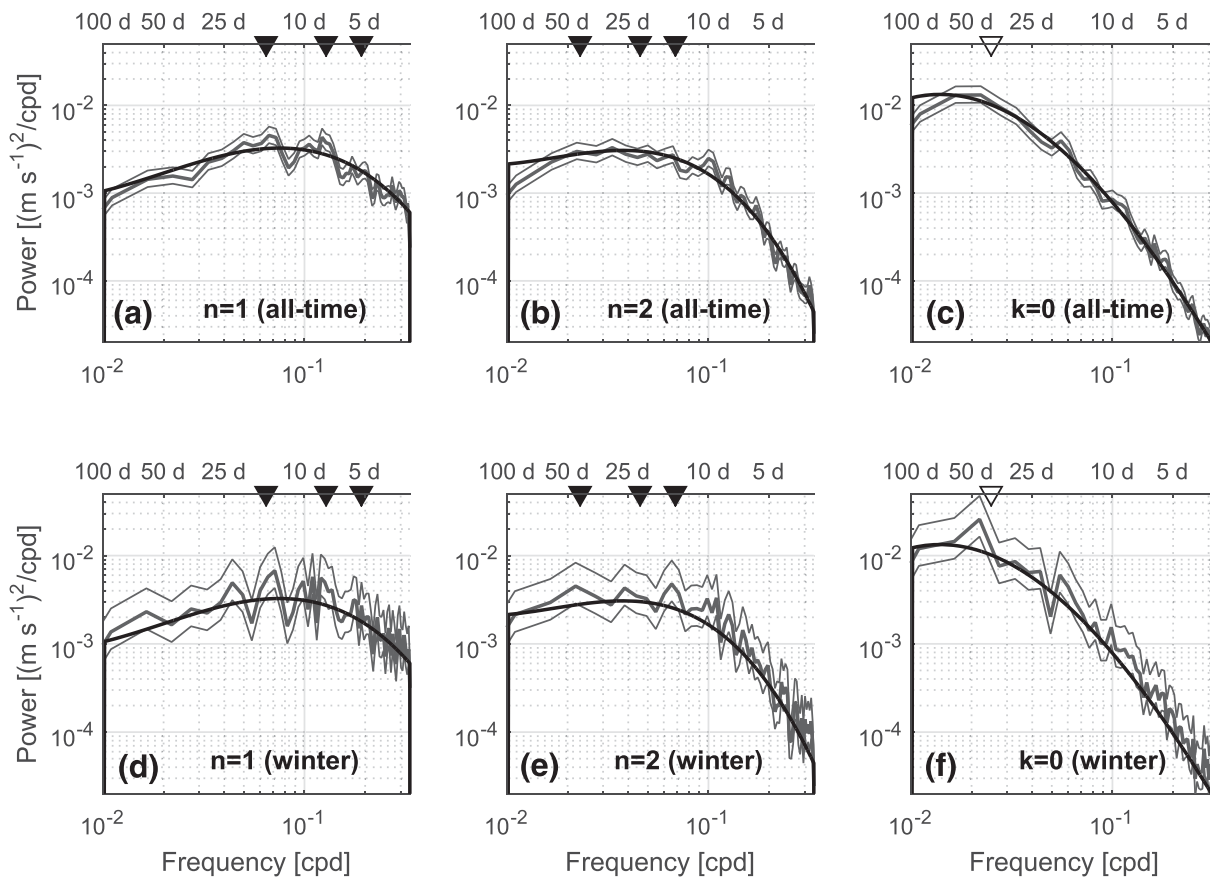


**Figure 9.** Power spectral estimates of the predicted signals. (a) Power spectrum for the  $n = 1$  signal (bold gray) with 90% confidence interval (thin gray). For assessment of statistical significance, a null spectrum is estimated by fitting a cubic polynomial to the log-transformed spectrum (bold black). Expected resonances at wavenumbers 1–3 are indicated (black wedges). (b) As in (a) but for the  $n = 2$  signal. (c) As in (a) but for the wavenumber zero mode, where an empirical peak is indicated (hollow wedge). (d) Power spectrum for wintertime  $n = 1$  velocity signal (bold gray) with 90% confidence interval (thin gray) and the same null spectrum from (a) (bold black). (e) As in (d) but for the  $n = 2$  signal and with the null spectrum from (b). (f) As in (d) but for the wavenumber zero mode and with the null spectrum from (c).

Predictions of velocity at 200.140 and SSH at Faraday/Vernadsky are similarly assessed (correlations in Table 2). The quality of prediction at 200.140 is similar to that at 300.100 with 47% of the total variance explained. For Faraday/Vernadsky SSH, correlation coefficients are not as good as those for velocity, likely due to our assumption that the SSH anomaly at the domain edge is zero, which changes the nodal points of the mode. On average, only 35% of the SSH variance can be explained. As was the case at 300.100, for both of these sites, when summing the wavenumber zero mode with the first two BSW, coherency is significant over most of the spectrum with small phase lag.

#### 5.4. Properties of the Predictions

We estimate the power spectral density of the  $n = 1$ ,  $n = 2$ , and wavenumber zero mode signals over the entire range of prediction (2008–2017) for all time and for winters only (May–October) in Figure 9. The spectra over all time use 50% overlapping 180-day Hanning windows while the winter-only spectra average all of the 183-day unwindowed May–October spectra (10 spectra). The first mode BSW spectrum has largest amplitude at the middle of the frequency range. Superimposed atop that background spectrum are three peaks, one each at periods near  $\sim 15.5$ ,  $\sim 7.8$ , and  $\sim 5.2$  days (black wedges in panel a), the former two of which are significant at a 10% level. Assuming a wavelength equal to the circumference of the Earth at  $67^\circ\text{S}$  (15,641 km), these periods correspond to integer wavenumbers of 1, 2, and 3. The second mode BSW spectrum is shifted towards lower frequency. There are no apparent peaks in the all-time spectrum (Figure 9b); however, there are peaks at periods near  $\sim 43.4$ ,  $\sim 21.7$ , and  $\sim 14.5$  days in the winter-only spectrum (the first

and last of which are barely significant at a 10% level; Figure 9e). Assuming the same circumpolar wavelength, these correspond to integer wavenumbers of 1, 2, and 3. The spectrum for the wavenumber zero mode is much redder and seems to peak at a period slightly longer than 40 days (Figures 9c and 9f, white wedge).

It can be shown that, when subject to linear damping, there is a response at both the forcing frequency and the free wave frequency (GS74). In the case that the wind system moves at the free wave speed ( $\omega \rightarrow kc_n$ ), resonance occurs. The peaks in the spectra can be interpreted as resonances with atmospheric variability. This is similar to the results of Kusahara and Ohshima (2009) who showed that BSW with  $k \leq 3$  were most pronounced at their resonant periods and were otherwise swamped by wavenumber zero variability. However, we have additionally shown that resonances are observed for the second mode BSW, albeit only in wintertime. Resonances for the second mode BSW are less pronounced because the mode's resonant frequencies (at  $k = 1-3$ ) are comparable to the inverse damping time scale ( $r_t \approx c_2k$ ) whereas the resonant frequencies for the first mode BSW are greater than the inverse damping time scale ( $r_t < c_1k$ ). In general, the resonant peaks are not always statistically significant because the forcing does not strictly include westward propagating variability and the ocean additionally responds at each forcing frequency (the smooth portion of the spectra).

## 6. Discussions

We have shown that the barotropic long-shore current observed on the WAP shelf consists of a wavenumber zero mode (Figure 5) and at least two BSW modes. Further, we have shown that these modes are forced by the long-shore wind stress, being able to predict on average about half of the total velocity variance at intra-seasonal time scales with nothing more than surface stress data (Figures 6–8; Table 2). Importantly, the predictions do a good job capturing both the phasing and the dimensional amplitude of the observed variability. The wavenumber zero mode is most energetic at increasingly low frequencies, as expected from its transfer function (equation 2), while the BSW tend to be slightly more apparent at periods where they may resonate with westward propagating atmospheric structures (Figure 9). Two additional findings are the importance of higher modal variability and the dominance of 40- to 60-day periods. We consider each of these findings in more detail and then discuss some implications for shelf-slope exchange.

### 6.1. Why Is the Second Mode BSW So Important?

An unexpected result of this study is the importance of the second mode BSW. This is evident from the quality of the wind-driven velocity predictions, which increases upon introduction of the second mode BSW (Table 2). The importance of the second mode may have been missed in earlier studies that focused on coastal SSH as its modal SSH amplitude is relatively small at the coast. On the other hand, it may have been missed because it is most energetic at periods that overlap with where the wavenumber zero mode is strong (40–60 days) or where the first mode BSW is also resonant (e.g., ~15 days; Figures 9a and 9b).

Part of the importance of the second mode BSW is determined directly from the bathymetry: its wind-coupling coefficient is comparable to that of the first mode wave (Figure 2a), and its amplitude at the mooring isobath is slightly larger than that of the first mode wave (Figure 3b), combining to give a similar amplitude factor ( $b_1u_1 \approx b_2u_2$ ). Going further, note that higher modes ( $n = 2, 3, \dots$ ) exist at (and are resonant at) a lower frequency for a given wavenumber than the first mode. Intraseasonal wind forcing with low wavenumber and low frequency is very energetic around the Antarctic margins (Matthews & Meredith, 2004; Pohl et al., 2010) and in the southeastern Pacific (Iijima et al., 2009; Mo & Higgins, 1998) as discussed in the next section.

### 6.2. Why Does Variability With Period 40–60 Days Dominate?

The power spectra of (and the coherency spectra with) the predicted wavenumber zero mode and the second mode BSW all have peaks at periods close to 40 days. The strength of spectral power varies interannually and is strongest in the winter, which is consistent with tropical teleconnection: Atmospheric Rossby wave propagation tends to occur primarily into the winter hemisphere (Kiladis & Mo, 1998). A period of ~40 days is consistent with intraseasonal tropical teleconnection via the Madden-Julian Oscillation (MJO). Variability in Drake Passage transport with period 30-70 days has been attributed to the MJO (Matthews & Meredith, 2004). While those authors attributed the increase in ACC transport at ~40-day period to a

modulation of SAM-like, zonally symmetric forcing by the MJO, there is some debate as to whether or not the MJO and SAM interact at all. Pohl et al. (2010) suggest that the MJO anomalies manifest with more of a dipolar (wavenumber 1) structure and suggest that the variance with 40-day period might be due to variability intrinsic to the SAM.

The leading EOFs of intraseasonal atmospheric variability represent the Pacific-South American (PSA) pattern with a period near 40 days (e.g., Iijima et al., 2009; Mo & Higgins, 1998). The PSA pattern consists of an approximately wavenumber 3 sequence of alternating cyclones and anticyclones that carry the teleconnection to the Antarctic and its amplitude is largest in the southern Pacific/South America region (Mo & Higgins, 1998). While the PSA pattern can originate from the MJO in austral winter (Kiladis & Mo, 1998), it may have different origin and only episodically interact with tropical convection (Mo & Higgins, 1998). The large center of action in the southeastern Pacific suggests the potential for a strong imprint on WAP SSH and currents. Heterogeneous correlation maps between long-shore velocity and SLP (McKee & Martinson, 2020) indicate strongest correlations in this vicinity. This may be because the damping associated with the second mode BSW is such that the length scale for memory of atmospheric forcing is only  $c_2/r_t \approx 1,800$  km, which is about the size of the alternating high and low pressure centers of the PSA. That is, the spatial memory of the second mode BSW is the same size as regular atmospheric variability.

In short, in the 40- to 60-day range, atmospheric variability potentially associated with the MJO may project onto the wavenumber zero mode whose transfer function permits response at arbitrary frequency, may resonate with the second mode BSW at wavenumber 1, or may project onto the second mode BSW with disproportionate influence on the WAP due to the PSA's large center of action there and the second mode's frictional damping scale.

### 6.3. Implication: Upwelling at a Coastal Canyon Head

Canyon heads on the WAP are ecological hotspots coincident with locations of permanent Adelie penguin breeding sites and increased phytoplankton biomass (Ducklow et al., 2007; Fraser & Trivelpiece, 1996; Schofield et al., 2013). Compared to the adjacent shelf, coastal submarine canyons have reduced sea ice, elevated sea surface temperature, elevated chlorophyll, and an elevated abundance of diatoms (Kavanaugh et al., 2015). The coincidence of canyon heads with reduced sea ice and elevated sea surface temperature suggests that mechanical shoaling of warm water places a physical control on the environment. This is consistent with the annual bloom not being initially limited by macronutrients (Kim et al., 2016) and instead being more sensitive to mixed layer depth (Carvalho et al., 2016). Recent results from an ocean observing system suggest residence times associated with advection by surface currents are about 1 to 2 days, which is shorter than phytoplankton doubling time growth rates (Kohut et al., 2018).

Pal E (158 m depth) is situated at the edge of the Palmer coastal environment, adjacent to the slope leading into Palmer Deep canyon (1,400 m), thus rendering it an ideal location to test communication between the two regions. The summer water column exhibits a warm seasonal mixed layer, but by the onset of winter, the entire column is mixed to near the freezing point (Figure 10a). Crucially, the homogenous freezing water in winter is punctuated by episodic, bottom-driven warming events with period near 40 days (Figure 10b). Because the warming is bottom intensified and the surface remains near the freezing point, the signal must originate from deeper in the canyon.

The time series of near-bottom (120 dbar) intraseasonal temperature at Pal E is significantly correlated ( $p \approx 0$ ) to the predicted SSH (wavenumber zero mode plus first and second mode BSW) at short lag ( $r = -0.38$ , lag = 4.5 days; Figure 10c). The correlation improves if we consider the wavenumber zero mode only ( $r = -0.43$ , lag = 5.5 days). We hypothesize that the enhanced barotropic circulation steers flow through the network of canyons towards the coast to force upwelling at the canyon head (e.g., Kämpf, 2006; see McKee & Martinson, 2020). The process mechanically shoals the pycnocline which may reduce the mixed layer depth assuming no change to surface fluxes. A major novel result is the finding that bathymetric features can link very disparate length scales of wind forcing and upwelling response.

### 6.4. Implication: Isopycnal Displacement at the Shelf Edge

McKee and Martinson (2020) showed that barotropic velocity fluctuations and subpycnocline temperature on the WAP are generally incoherent. The incoherence was explained by noting that, while velocity variance is dominated by wind-driven, large-scale, quasi-barotropic fluctuations, thermal variance is dominated by

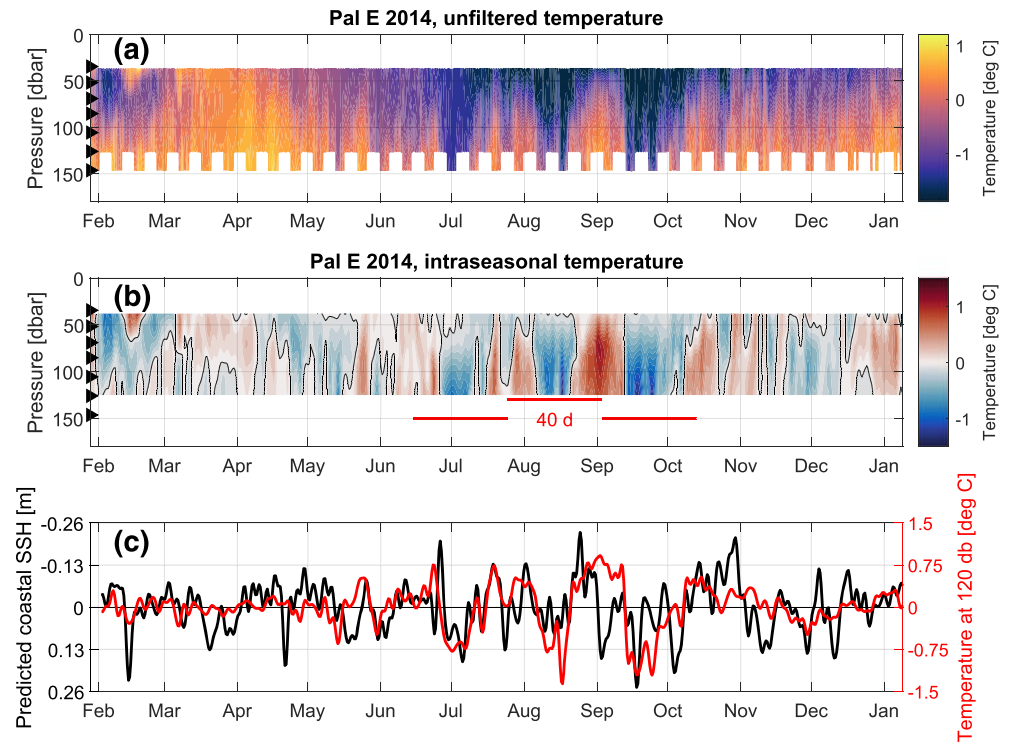


**Figure 10.** Upwelling signal at Pal E. (a) Time series of temperature profiles. The nominal thermistor depths are indicated at left. (b) The temperature profiles from (a) band-pass filtered in time to retain periods 3–100 days ( $0^{\circ}\text{C}$  temperature anomaly contour shown). The three red lines are each 40 days long, cumulatively increasing from 15 June 2014. (c) The filtered temperature signal at 120 dbar from panel (b) (red) plotted with the predicted coastal SSH anomaly at the 600 line (black; axis flipped).

small-scale mesoscale features (Graham et al., 2016; Martinson & McKee, 2012; McKee et al., 2019). An exception to this incoherence occurs at periods in the 40- to 60-day range, for which the long-shore current and the temperature maximum ( $T_{\text{max}}$ ) are weakly anticorrelated. This study shows that the second mode CTW is energetic in that range and is most baroclinic over the steep continental slope.

The second mode CTW potential density for WAP bathymetry is bottom trapped and confined to the steepest portion of the slope. Thus, the waves could conceivably displace an isopycnal near the climatological  $T_{\text{max}}$ , which is at mid-depth. This is similar to the phenomenon observed by Griffin and Middleton (1986) who observed second mode CTW to yield thermocline excursions of  $\sim 30$  m over the slope. Therefore, a consequence of the second mode CTW is the ability to enhance or suppress warm water access to the continental shelf. This observation may be related to undercurrents observed under the Antarctic Slope Front (e.g., Chavanne et al., 2010; Walker et al., 2013), explaining their origin and associated isotherm displacements in terms of the arrival of the second mode wave (Middleton & Cirano, 1999; Sugihara, 1982). Further, because isopycnals shoal uniformly over the continental slope (e.g., see S4P in Orsi & Whitworth, 2005), the isopycnal excursions also displace the location of steepest isopycnal slope offshore, potentially mitigating eddy stirring of heat across the slope by changing the ratio of isopycnal slope to topographic slope. This is relevant because the growth time scale of instabilities in this environment is much faster than the wave period (McKee et al., 2019).

## 7. Conclusions

We have shown that about half of the intraseasonal (3–100 days) barotropic velocity variance on the WAP shelf can be explained by a wavenumber zero mode and at least two BSW modes forced by nothing more than surface stress. The wavenumber zero mode is most energetic at increasingly long periods with a peak at 40–50 days in winter. The first mode BSW is most energetic at periods 5–15 days with spectral peaks

where it may resonate with westward propagating atmospheric structures while the second mode is more energetic at lower frequencies with significant spectral peaks only in winter. Calculation of dispersive, stratified CTW modes suggests that the long-wave, barotropic approximations are good on intraseasonal time scales, although dispersion may account for some of the scatter in the predictions.

The wind-driven velocity fluctuations have major impacts on shelf-slope exchange. Firstly, the enhanced barotropic flow leads to episodic upwelling of warm water at an ecologically productive canyon head that may keep sea ice thin, may aggregate phytoplankton biomass, and may shoal the pycnocline. Secondly, the subtle wave baroclinicity over the steep continental slope yields isopycnal migrations near the depth of the temperature maximum. This latter effect is likely to be most pronounced in environments with steep slopes like the WAP.

While the existence of a wavenumber zero signal has been established by others through analysis of subsurface pressure data, the results here show observation of wavenumber zero and long BSW signals in ocean velocity data from an Antarctic shelf. Given its transfer function, we would expect wavenumber zero variability to dominate other mooring records at low frequency. While the BSW signal should conceivably exist elsewhere, it might be overemphasized on the WAP and perhaps Amundsen Sea shelves due to the proximity of strong, regular atmospheric variability. It will be important to understand how these signals may interact with other signals proposed to affect the barotropic velocity field (e.g., Kelvin waves; Spence et al., 2017), and further observations should aim to constrain their consequences for baroclinic conversion and scalar exchange at the shelf edge.

#### Acknowledgments

This manuscript is based on the graduate work of McKee. McKee and Martinson were supported by NSF grant PLR-1440435. Richard Iannuzzi designed and assembled the moorings and provided valuable comments. The ocean mooring data collected for this study are available at <https://doi.org/10.6073/pasta/74b690cd34d9d15d185fa6473ea2cf7>. All other existing data sources are referenced in section 3 of this paper.

#### References

- Aoki, S. (2002). Coherent sea level response to the Antarctic Oscillation. *Geophysical Research Letters*, *29*(20), 1950. <https://doi.org/10.1029/2002GL015733>
- Assmann, K. M., Jenkins, A., Shoosmith, D. R., Walker, D. P., Jacobs, S. S., & Nicholls, K. W. (2013). Variability of Circumpolar Deep Water transport onto the Amundsen Sea continental shelf through a shelf break trough. *Journal of Geophysical Research: Oceans*, *118*, 6603–6620. <https://doi.org/10.1002/2013JC008871>
- Brink, K. H. (1982a). A comparison of long coastal trapped wave theory with observations off Peru. *Journal of Physical Oceanography*, *12*(8), 897–913. [https://doi.org/10.1175/1520-0485\(1982\)012<0897:ACOLCT>2.0.CO;2](https://doi.org/10.1175/1520-0485(1982)012<0897:ACOLCT>2.0.CO;2)
- Brink, K. H. (1982b). The effect of bottom friction on low-frequency coastal trapped waves. *Journal of Physical Oceanography*, *12*(2), 127–133. [https://doi.org/10.1175/1520-0485\(1982\)012<0127:TEOBFO>2.0.CO;2](https://doi.org/10.1175/1520-0485(1982)012<0127:TEOBFO>2.0.CO;2)
- Brink, K. H. (2006). Coastal-trapped waves with finite bottom friction. *Dynamics of Atmospheres and Oceans*, *41*(3), 172–190. <https://doi.org/10.1016/j.jdynatmoce.2006.05.001>
- Brink, K. H., & Allen, J. S. (1978). On the effect of bottom friction on barotropic motion over the continental shelf. *Journal of Physical Oceanography*, *8*(5), 919–922. [https://doi.org/10.1175/1520-0485\(1978\)008<0919:OTEOBF>2.0.CO;2](https://doi.org/10.1175/1520-0485(1978)008<0919:OTEOBF>2.0.CO;2)
- Caldwell, P., Merrifield, M. A., & Thompson, P. R. (2015). Sea level measured by tide gauges from global oceans—the joint archive for sea level holdings (NCEI accession 0019568), version 5.5. NOAA National Centers for Environmental Information. Dataset. <https://doi.org/10.7289/V5V40S7W>
- Carvalho, F., Kohut, J., Oliver, M. J., Sherrell, R. M., & Schofield, O. (2016). Mixing and phytoplankton dynamics in a submarine canyon in the West Antarctic Peninsula. *Journal of Geophysical Research: Oceans*, *121*, 5069–5083. <https://doi.org/10.1002/2016JC011650>
- Chavanne, C. P., Heywood, K. J., Nicholls, K. W., & Fer, I. (2010). Observations of the Antarctic Slope Undercurrent in the southeastern Weddell Sea. *Geophysical Research Letters*, *37*, L13601. <https://doi.org/10.1029/2010GL043603>
- Cook, A. J., Holland, P. R., Meredith, M. P., Murray, T., Luckman, A., & Vaughan, D. G. (2016). Ocean forcing of glacier retreat in the western Antarctic Peninsula. *Science*, *353*(6296), 283–286. <https://doi.org/10.1126/science.aae0017>
- Dinniman, M. S., & Klinck, J. M. (2004). A model study of circulation and cross-shelf exchange on the West Antarctic Peninsula continental shelf. *Deep Sea Research Part II: Topical Studies in Oceanography*, *51*(17), 2003–2022. <https://doi.org/10.1016/j.dsr2.2004.07.030>
- Dinniman, M. S., Klinck, J. M., & Hofmann, E. E. (2012). Sensitivity of Circumpolar Deep Water transport and ice shelf basal melt along the West Antarctic Peninsula to changes in the winds. *Journal of Climate*, *25*(14), 4799–4816. <https://doi.org/10.1175/JCLI-D-11-00307.1>
- Dinniman, M. S., Klinck, J. M., & Smith, W. O. (2011). A model study of Circumpolar Deep Water on the West Antarctic Peninsula and Ross Sea continental shelves. *Deep Sea Research Part II: Topical Studies in Oceanography*, *58*(13), 1508–1523. <https://doi.org/10.1016/j.dsr2.2010.11.013>
- Ducklow, H. W., Baker, K., Martinson, D. G., Quetin, L. B., Ross, R. M., Smith, R. C., et al. (2007). Marine pelagic ecosystems: the West Antarctic Peninsula. *Philosophical Transactions of the Royal Society of London. Series B, Biological Sciences*, *362*(1477), 67–94. <https://doi.org/10.1098/rstb.2006.1955>
- European Centre for Medium-range Weather Forecast. (2011). The ERA-interim reanalysis dataset. Copernicus Climate Change Service (C3S). <https://www.ecmwf.int/en/forecasts/datasets/reanalysis-datasets/era-interim>
- Fraser, W. R., & Trivelpiece, W. Z. (1996). Factors controlling the distribution of seabirds: Winter-summer heterogeneity in the distribution of Adélie penguin populations. In R. M. Ross, E. E. Hofmann, & L. B. Quetin (Eds.), *Foundations for Ecological Research West of the Antarctic Peninsula* (Vol. 70, pp. 257–272). Washington, DC: American Geophysical Union (AGU). <https://doi.org/10.1029/AR070p0257>
- Gill, A. E. (1982). *Atmosphere-Ocean Dynamics*, (1st ed.). New York, NY: Academic Press.
- Gill, A. E., & Schumann, E. H. (1974). The generation of long shelf waves by the wind. *Journal of Physical Oceanography*, *4*(1), 83–90. [https://doi.org/10.1175/1520-0485\(1974\)004<0083:TGOLSW>2.0.CO;2](https://doi.org/10.1175/1520-0485(1974)004<0083:TGOLSW>2.0.CO;2)

- Gordon, R. L., & Huthnance, J. M. (1987). Storm-driven continental shelf waves over the Scottish continental shelf. *Continental Shelf Research*, 7(9), 1015–1048. [https://doi.org/10.1016/0278-4343\(87\)90097-5](https://doi.org/10.1016/0278-4343(87)90097-5)
- Graham, J. A., Dinniman, M. S., & Klinck, J. M. (2016). Impact of model resolution for on-shelf heat transport along the West Antarctic Peninsula. *Journal of Geophysical Research: Oceans*, 121, 7880–7897. <https://doi.org/10.1002/2016JC011875>
- Griffin, D. A., & Middleton, J. H. (1986). Coastal-trapped waves behind a large continental shelf island, southern Great Barrier Reef. *Journal of Physical Oceanography*, 16(10), 1651–1664. [https://doi.org/10.1175/1520-0485\(1986\)016<1651:CTWBAL>2.0.CO;2](https://doi.org/10.1175/1520-0485(1986)016<1651:CTWBAL>2.0.CO;2)
- Hughes, C. W., Meredith, M. P., & Heywood, K. J. (1999). Wind-driven transport fluctuations through Drake Passage: A southern mode. *Journal of Physical Oceanography*, 29(8), 1971–1992. [https://doi.org/10.1175/1520-0485\(1999\)029<1971:WDTFTD>2.0.CO;2](https://doi.org/10.1175/1520-0485(1999)029<1971:WDTFTD>2.0.CO;2)
- Hughes, C. W., Woodworth, P. L., Meredith, M. P., Stepanov, V., Whitworth, T., & Pyne, A. R. (2003). Coherence of Antarctic sea levels, Southern Hemisphere Annular Mode, and flow through Drake Passage. *Geophysical Research Letters*, 30(9), 1464. <https://doi.org/10.1029/2003GL017240>
- Huthnance, J. M. (1978). On coastal trapped waves: Analysis and numerical calculation by inverse iteration. *Journal of Physical Oceanography*, 8(1), 74–92. [https://doi.org/10.1175/1520-0485\(1978\)008<0074:OCTWAA>2.0.CO;2](https://doi.org/10.1175/1520-0485(1978)008<0074:OCTWAA>2.0.CO;2)
- Huthnance, J. M. (1981). Waves and currents near the continental shelf edge. *Progress in Oceanography*, 10(4), 193–226. [https://doi.org/10.1016/0079-6611\(81\)90004-5](https://doi.org/10.1016/0079-6611(81)90004-5)
- Iijima, Y., Aoki, S., & Kutsuwada, K. (2009). The Southern Annular Mode and opposite-phased Basin Mode of the Southern Ocean circulation. *Journal of Oceanography*, 65(1), 53–60. <https://doi.org/10.1007/s10872-009-0005-0>
- Jensen, M. F., Fer, I., & Darelus, E. (2013). Low frequency variability on the continental slope of the southern Weddell Sea. *Journal of Geophysical Research: Oceans*, 118, 4256–4272. <https://doi.org/10.1002/jgrc.20309>
- Kämpf, J. (2006). Transient wind-driven upwelling in a submarine canyon: A process-oriented modeling study. *Journal of Geophysical Research*, 111, C11011. <https://doi.org/10.1029/2006JC003497>
- Kavanaugh, M. T., Abdala, F. N., Ducklow, H., Glover, D., Fraser, W., Martinson, D., et al. (2015). Effect of continental shelf canyons on phytoplankton biomass and community composition along the western Antarctic Peninsula. *Marine Ecology Progress Series*, 524, 11–26. <https://doi.org/10.3354/meps11189>
- Kiladis, G. N., & Mo, K. C. (1998). Interannual and intraseasonal variability in the southern hemisphere. In D. J. Karoly, & D. G. Vincent (Eds.), *Meteorology of the Southern Hemisphere*, (Vol. 49, pp. 307–336). Boston, MA: American Meteorological Society. [https://doi.org/10.1007/978-1-935704-10-2\\_11](https://doi.org/10.1007/978-1-935704-10-2_11)
- Kim, H., Doney, S. C., Iannuzzi, R. A., Meredith, M. P., Martinson, D. G., & Ducklow, H. W. (2016). Climate forcing for dynamics of dissolved inorganic nutrients at Palmer Station, Antarctica: An interdecadal (1993–2013) analysis. *Journal of Geophysical Research: Biogeosciences*, 121, 2369–2389. <https://doi.org/10.1002/2015JG003311>
- Kohut, J. T., Winsor, P., Statscewich, H., Oliver, M. J., Fredj, E., Couto, N., et al. (2018). Variability in summer surface residence time within a West Antarctic Peninsula biological hotspot. *Philosophical Transactions of the Royal Society. Series A, Mathematical, Physical, and Engineering Sciences*, 376(2122). <https://doi.org/10.1098/rsta.2017.0165>
- Kusahara, K., & Ohshima, K. I. (2009). Dynamics of the wind-driven sea level variation around Antarctica. *Journal of Physical Oceanography*, 39(3), 658–674. <https://doi.org/10.1175/2008JPO3982.1>
- Kusahara, K., & Ohshima, K. I. (2014). Kelvin waves around Antarctica. *Journal of Physical Oceanography*, 44(11), 2909–2920. <https://doi.org/10.1175/JPO-D-14-0051.1>
- Locarnini, R. A., Mishonov, A. V., Baranova, O. K., Boyer, T. P., Zweng, M. M., Garcia, H. E., et al. (2018). World Ocean Atlas 2018, volume 1: Temperature. NOAA Atlas NESDIS 81, 45 Pp. NOAA National Centers for Environmental Information Ocean Climate Laboratory.
- Martinson, D. G. (2020). Data from Oceanographic Moorings Deployed on the Antarctic Continental Shelf (and Inshore) West of the Antarctic Peninsula as Part of the Palmer Long Term Ecological Research Project (PAL LTER), 2007–2017. Environmental Data Initiative. <https://doi.org/10.6073/pasta/74b690cd34d9d15d185fa6473ea2cf7>
- Martinson, D. G., & McKee, D. C. (2012). Transport of warm Upper Circumpolar Deep Water onto the western Antarctic Peninsula continental shelf. *Ocean Science*, 8(4), 433–442. <https://doi.org/10.5194/os-8-433-2012>
- Martinson, D. G., Stammerjohn, S. E., Iannuzzi, R. A., Smith, R. C., & Vernet, M. (2008). Western Antarctic Peninsula physical oceanography and spatio-temporal variability. *Deep Sea Research Part II: Topical Studies in Oceanography*, 55(18), 1964–1987. <https://doi.org/10.1016/j.dsr2.2008.04.038>
- Matthews, A. J., & Meredith, M. P. (2004). Variability of Antarctic circumpolar transport and the Southern Annular Mode associated with the Madden-Julian Oscillation. *Geophysical Research Letters*, 31, L24312. <https://doi.org/10.1029/2004GL021666>
- McKee, D. C., & Martinson, D. G. (2020). Spatially coherent intraseasonal velocity fluctuations on the Western Antarctic Peninsula shelf. *Journal of Geophysical Research Oceans*, 125, e2019JC015770. <https://doi.org/10.1029/2019JC015770>
- McKee, D. C., Martinson, D. G., & Schofield, O. (2019). Origin and attenuation of mesoscale structure in Circumpolar Deep Water intrusions to an Antarctic shelf. *Journal of Physical Oceanography*, 49(5), 1293–1318. <https://doi.org/10.1175/JPO-D-18-0133.1>
- Middleton, J. F., & Cirano, M. (1999). Wind-forced downwelling slope currents: A numerical study. *Journal of Physical Oceanography*, 29(8), 1723–1743. [https://doi.org/10.1175/1520-0485\(1999\)029<1723:WFDSCA>2.0.CO;2](https://doi.org/10.1175/1520-0485(1999)029<1723:WFDSCA>2.0.CO;2)
- Middleton, J. H., Foster, T. D., & Foldvik, A. (1987). Diurnal shelf waves in the southern Weddell Sea. *Journal of Physical Oceanography*, 17(6), 784–791. [https://doi.org/10.1175/1520-0485\(1987\)017<0784:DSWITS>2.0.CO;2](https://doi.org/10.1175/1520-0485(1987)017<0784:DSWITS>2.0.CO;2)
- Mo, K. C., & Higgins, R. W. (1998). The Pacific–South American modes and tropical convection during the southern hemisphere winter. *Monthly Weather Review*, 126(6), 1581–1596. [https://doi.org/10.1175/1520-0493\(1998\)126<1581:TPSAMA>2.0.CO;2](https://doi.org/10.1175/1520-0493(1998)126<1581:TPSAMA>2.0.CO;2)
- National Geophysical Data Center. (1988). Digital relief of the surface of the earth. Data Announcement 88-MGG-02, NOAA, National Geophysical Data Center.
- National Oceanography Centre. (2015). Bottom Pressure Deployments at Drake Passage South Deep. Permanent Service for Mean Sea Level. Retrieved from [https://www.psmsl.org/data/bottom\\_pressure/locations/1608.php](https://www.psmsl.org/data/bottom_pressure/locations/1608.php)
- Naveira Garabato, A. C., Dotto, T. S., Hooley, J., Bacon, S., Tsamados, M., Ridout, A., et al. (2019). Phased response of the subpolar Southern Ocean to changes in circumpolar winds. *Geophysical Research Letters*, 46, 6024–6033. <https://doi.org/10.1029/2019GL082850>
- Orsi, A. H., & Whitworth, T. (2005). Hydrographic Atlas of the World Ocean Circulation Experiment (WOCE) Volume 1: Southern Ocean. WOCE International Project Office.
- Pawlowicz, R., Beardsley, B., & Lentz, S. (2002). Classical tidal harmonic analysis including error estimates in MATLAB using T\_TIDE. *Computers & Geosciences*, 28(8), 929–937. [https://doi.org/10.1016/S0098-3004\(02\)00013-4](https://doi.org/10.1016/S0098-3004(02)00013-4)
- Pohl, B., Fauchereau, N., Reason, C. J. C., & Rouault, M. (2010). Relationships between the Antarctic Oscillation, the Madden–Julian Oscillation, and ENSO, and consequences for rainfall analysis. *Journal of Climate*, 23(2), 238–254. <https://doi.org/10.1175/2009JCLI2443.1>

- Rivas, D. (2017). Wind-driven coastal-trapped waves off southern Tamaulipas and northern Veracruz, western Gulf of Mexico, during winter 2012–2013. *Estuarine, Coastal and Shelf Science*, *185*, 1–10. <https://doi.org/10.1016/j.ecss.2016.12.002>
- Schmidtko, S., Heywood, K. J., Thompson, A. F., & Aoki, S. (2014). Multidecadal warming of Antarctic waters. *Science*, *346*(6214), 1227–1231. <https://doi.org/10.1126/science.1256117>
- Schofield, O., Ducklow, H., Bernard, K., Doney, S., Patterson-Fraser, D., Gorman, K., et al. (2013). Penguin biogeography along the West Antarctic Peninsula: Testing the canyon hypothesis with Palmer LTER observations. *Oceanography*, *26*(3), 204–206. <https://doi.org/10.5670/oceanog.2013.63>
- Schulz, W. J., Mied, R. P., & Snow, C. M. (2012). Continental shelf wave propagation in the Mid-Atlantic Bight: A general dispersion relation. *Journal of Physical Oceanography*, *42*(4), 558–568. <https://doi.org/10.1175/JPO-D-11-098.1>
- Spence, P., Holmes, R. M., Hogg, A. M., Griffies, S. M., Stewart, K. D., & England, M. H. (2017). Localized rapid warming of West Antarctic subsurface waters by remote winds. *Nature Climate Change*, *7*(8), 595–603. <https://doi.org/10.1038/nclimate3335>
- St-Laurent, P., Klinck, J. M., & Dinniman, M. S. (2013). On the role of coastal troughs in the circulation of warm Circumpolar Deep Water on Antarctic shelves. *Journal of Physical Oceanography*, *43*(1), 51–64. <https://doi.org/10.1175/JPO-D-11-0237.1>
- Suginohara, N. (1982). Coastal upwelling: Onshore–offshore circulation, equatorward coastal jet and poleward undercurrent over a continental shelf-slope. *Journal of Physical Oceanography*, *12*(3), 272–284. [https://doi.org/10.1175/1520-0485\(1982\)012<0272:CUOCEC>2.0.CO;2](https://doi.org/10.1175/1520-0485(1982)012<0272:CUOCEC>2.0.CO;2)
- Thoma, M., Jenkins, A., Holland, D., & Jacobs, S. (2008). Modelling Circumpolar Deep Water intrusions on the Amundsen Sea continental shelf, Antarctica. *Geophysical Research Letters*, *35*, L18602. <https://doi.org/10.1029/2008GL034939>
- Wählin, A. K., Kalén, O., Arneborg, L., Björk, G., Carvajal, G. K., Ha, H. K., et al. (2013). Variability of warm deep water inflow in a submarine trough on the Amundsen Sea shelf. *Journal of Physical Oceanography*, *43*(10), 2054–2070. <https://doi.org/10.1175/JPO-D-12-0157.1>
- Wählin, A. K., Kalén, O., Assmann, K. M., Darelus, E., Ha, H. K., Kim, T. W., & Lee, S. H. (2016). Subinertial oscillations on the Amundsen Sea shelf, Antarctica. *Journal of Physical Oceanography*, *46*(9), 2573–2582. <https://doi.org/10.1175/JPO-D-14-0257.1>
- Wählin, A. K., Muench, R. D., Arneborg, L., Björk, G., Ha, H. K., Lee, S. H., & Alsén, H. (2012). Some implications of Ekman layer dynamics for cross-shelf exchange in the Amundsen Sea. *Journal of Physical Oceanography*, *42*(9), 1461–1474. <https://doi.org/10.1175/JPO-D-11-041.1>
- Walker, D. P., Jenkins, A., Assmann, K. M., Shoosmith, D. R., & Brandon, M. A. (2013). Oceanographic observations at the shelf break of the Amundsen Sea, Antarctica. *Journal of Geophysical Research: Oceans*, *118*, 2906–2918. <https://doi.org/10.1002/jgrc.20212>
- Webb, D. J., Holmes, R. M., Spence, P., & England, M. H. (2019). Barotropic kelvin wave-induced bottom boundary layer warming along the West Antarctic Peninsula. *Journal of Geophysical Research: Oceans*, *124*, 1595–1615. <https://doi.org/10.1029/2018JC014227>
- Weijer, W., & Gille, S. T. (2005). Adjustment of the Southern Ocean to wind forcing on synoptic time scales. *Journal of Physical Oceanography*, *35*(11), 2076–2089. <https://doi.org/10.1175/JPO2801.1>
- Zweng, M. M., Reagan, J. R., Seidov, D., Boyer, T. P., Locarnini, R. A., Garcia, H. E., et al. (2018). World Ocean Atlas 2018, volume 2: Salinity. NOAA Atlas NESDIS 82, 40 Pp. NOAA National Centers for Environmental Information Ocean Climate Laboratory.